The Design, Fabrication, and Modeling of a Piezoelectric Linear Motor

by

Mark E. Vaughan

Thesis submitted to the Faculty of the
Virginia Polytechnic Institute and State University
in partial fulfillment of the requirements for the degree of

Master of Science

in

Mechanical Engineering

Donald J. Leo, Chair
Mehdi Ahmadian
Harry H. Robertshaw

December 2001

Blacksburg, Virginia

For my parents,

Donald and Martha,

and my best friend,

Diana

The Design, Fabrication, and Modeling of a Piezoelectric Linear Motor

Mark E. Vaughan, M.S.
Virginia Polytechnic Institute and State University, 2001
Advisor: Donald J. Leo

Abstract

The focus of this research was to create a linear motor that could easily be packaged and still perform the same task of the current DC motor linear device. An incremental linear motor design was decided upon, for its flexibility in which the motor can be designed. To replace the current motor it was necessary to develop a high force, high speed incremental linear motor. To accomplish this task, piezoelectric actuators were utilized to drive the motor due their fast response times and high force capabilities.

The desired overall objectives of the research is to create an incremental linear motor with the capability of moving loads up to one hundred pounds and produce a velocity well over one inch per second. To aid the design process a lumped parameter model was created to simulate the motor's performance for any design parameter. Discrepancies occurred between the model and the actual motor performance for loads above 9.1 kilograms (20 pounds). The resulting model, however, was able to produce a good approximation of the motor's performance for the unloaded and lightly loaded cases.

The phase one design was limited by time constraints so a relatively low risk design was produced. The resulting incremental linear motor produced a velocity of 4.9 mm/sec (0.2 in/sec) at a drive frequency of 50 Hz. The velocity of the motor was limited by the drive frequency that the amplifiers could produce. The motor was found to produce a respectable stall load of 17 kilograms (38 pounds). The stall load of the phase one design was severely limited by clearance losses. An analysis of the motor's performance was conducted, possible improvements and future work recommendations for a phase two design are presented.

The Design, Fabrication, and Modeling of a Piezoelectric Linear Motor

Approved by
Advising Committee:

_____

_____

_____

Acknowledgments

First I would like to thank my advisor, Dr. Donald J. Leo, for his guidance during the course of this work. He has been an excellent teacher and means of encouragement making my learning experience at Virginia Tech an enjoyable one. I want to thank my colleagues in the Center for Intelligent Material Systems and Structures (CIMSS) for their help during my graduate work. Recognition should be given to Shannon Mauck for his invaluable assistance during the design process. I would also like to extend my thanks to Dr. Mehdi Admadian and Dr. Harry H. Robertshaw for their support as members of my advisor committee.

My sincere appreciation goes out to Diana Maphis. She supported my decision to continue with school, even though it meant a year and a half apart from each other. Her constant encouragement and support during the stressful times of my graduate work was invaluable.

Most importantly, I would like to thank my parents, Donald and Martha. My parents have always been there for me and have supported me through out my entire academic career. Without their continued love and support, I could not have accomplished what I have. I like to finish by thanking my sister, Cindy. She provided a helping hand when I first transferred to Virginia Tech and got me started off on the right foot.

Mark E. Vaughan

Virginia Polytechnic Institute and State University

December 2001

Contents

List of Tables

List of Figures

Nomenclature

um - microns

Vel - velocity

Δ - step size

f - drive frequency

$M1$ - mass of Brake 1

$M2$ - mass of Brake 2

$X1$ - displacement of Brake 1

$X2$ - displacement of Brake 2

$\dot{X}1$ - velocity of Brake 1

$\dot{X}2$ - velocity of Brake 2

$\ddot{X}1$ - acceleration of Brake 1

$\ddot{X}2$ - acceleration of Brake 2

Ke_{act} - stiffness of extending actuator

Kv_{act} - voltage coefficient of extending actuator

F_{act} - force generated by extending actuator

C_{act} - damping coefficient of extending actuator

V_{act} - voltage applied to extending actuator

m_{act} - mass of extending actuator

Kv_{brake} - voltage coefficient for brakes

V_{brake} - voltage applied to brakes

F_{brake1} - frictional force generated by Brake 1

F_{brake2} - frictional force generated by Brake 2

μ - frictional coefficient

m - mass of load

g - gravitational constant

Ke_{pzt} - stiffness of PZT actuator in amplified actuator

Kv_{pzt} - voltage coefficient of PZT actuator in amplified actuator

F_{pzt} - force produced by PZT actuator in amplified actuator

K_{comp} - stiffness of compliant structure

$L2/L1$ - gain of compliant structure

ω_{res} - resonant frequency

ζ - damping ratio

C - capacitance

I_{drive} - drive current

T_r - rise time

Chapter 1

Introduction

A piezoelectric linear motor using an inchworm type method of motion has been designed and fabricated with assistance from Don Leo and Shannon Mauck. In an effort to predict the operation of the linear motor under various conditions a lumped parameter model has been created. The following chapters will provide an overview of the design process, model verification, and resulting motor performance.

1.1 Motivation

With the development of modern industry, linear motors have been gaining popularity in several fields (optics, aircraft, biomedical, manufacturing, etc.). The popularity increase has been attributed to a need for highly precise positioning devices with short response times. Designers have found that by using linear motors, more travel can be produced in the same envelope. Currently there are many different classes of linear motors. The linear motors of interest in this paper make use of piezoelectric ceramic materials to develop precision positioning devices.

Piezoelectric linear motors have been created using a wide variety of different methods. This ability to create a variety of piezoelectric linear motors is due to the versatility a designer has when using piezoelectric ceramics. Piezoelectric ceramics can be purchased in many different shapes and sizes, allowing for flexibility during the design process. This versatility when designing a piezoelectric linear motor has a great advantage over traditional linear motors. As a result many piezoelectric linear motors have been designed with a specific application in mind.

One technique of creating a piezoelectric linear motor uses an inchworm type method of motion. The inchworm type linear motor is known to produce high forces, accurate positioning, and large displacements limited only by the length of the guide channel. These piezoelectric motors can be designed relatively small and light, due to the large force capabilities of piezoelectric ceramic material. One of the most favorable aspects of the inchworm motor is its ability to be integrated into the structure of the mechanical device to be moved. For example, the inchworm motor can be designed to mount in a preexisting guide channel for a mechanical device. The inchworm technique also allows the linear motor to change directions by simply switching the clamping cycles. The result is a high force, bi-directional motor that can be easily packaged.

1.2 The Piezoelectric Concept

1.2.1 History

The history of piezoelectric materials date back to 1880, when Pierre and Jacques Curie published the first experimental demonstration of piezoelectricity in various materials such as: rochelle salt, quartz, and tourmaline [Shields (1966); Piezo_Systems (2000)]. In nature the piezoelectric phenomenon occurs when one form of energy is transformed into another form. For various materials, piezoelectricity can be observed as an electric charge generated by a material when a mechanical pressure is applied to the material (Figure 1.1a). The opposite effect can also be observed as a physical deformation of the material due to an applied electrical charge to the material (Figure 1.1b).

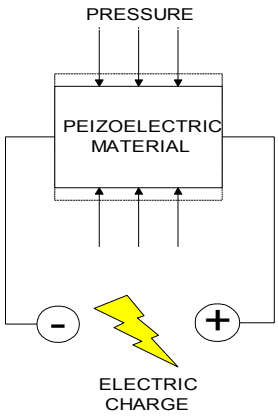

Figure 1.1a: Charge generated by applied pressure.

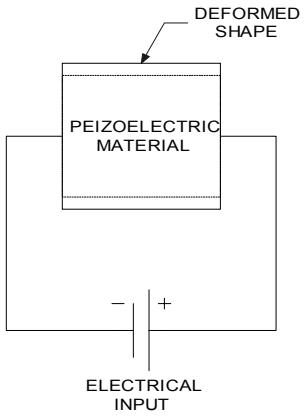

Figure 1.1b: Change in shape when voltage is applied.

1.2.2 Synthetic Materials

The natural piezoelectric materials were found to provide good piezoelectric characteristics, however they had limitations. The upper temperature limit (curie point) of these natural materials is relatively low, with the exception of quartz. These natural materials are also limited by the amount of energy that they can withstand. In 1940 Arthur von Hiffel produced the first synthetic piezoelectric material. He was able to acquire piezoelectric properties from barium titanate after subjecting the material to an electric current (polarization) [Shields (1966)]. The development of barium titanate then led to the discovery of other synthetic piezoelectric materials. One such material consists of lead titanate zirconate (PZT). PZT ceramics are currently the most readily available piezoelectric materials in today's market. PZT ceramics offer favorable characteristics such as: high force capabilities, an upper temperature limit of 300 degrees Celsius, and a maximum strain of 0.1%.

1.3 Literature Survey of Inchworm Type Linear Motors

To learn and gain experience from previous inchworm designs, an extensive literature survey of papers and patents was conducted. The literature survey provides an overview of a multiple of methods used to create inchworm motors, demonstrating the versatility of the inchworm design process.

All inchworm motors presented in this survey use the same technique of small repetitive increments to produce large movements. However, the methods to produce the small increments can be categorized into three different categories. The first category is the "piezoelectric" inchworm motor, in which both the extending and the clamping mechanisms are constructed of piezoelectric actuators. The second category is the "magnetostrictive" inchworm motor, in which both the extending and the clamping mechanisms are constructed of magnetostrictive actuators. The last category is the "hybrid" inchworm motor, in which the extending and the clamping mechanisms are constructed of the two different types of actuators.

The inchworm motors presented in this survey can also be separated by the method in which the large movements are produced. There are basically three different types of actuation techniques. The first technique can be referred to as a "walker", in which the both the extending and the clamping mechanisms moving along a guiding shaft. Here the

structure appears to be walking along the path of actuation. The second technique can be referred to as a "pusher", in which the extending and clamping mechanisms remain stationary. Here the structure appears to push the shaft along the path of actuation. The third technique referred to as the hybrid "walker-pusher", in which either the extending or the clamping mechanism moves along the shaft while the other mechanism remains stationary.

The literature survey conducted found inchworm type linear motors dating back to 1964. The designers of these early inchworm type motors were pioneers to the technique laying down a foundation for future designs to come. One of these early designs was presented by G.R. Stibitz (1964). This design of a magnetostrictive motor makes use of the "pusher" technique as the method of actuation. The design employs three stationary frictional restraints and extending mechanisms to produce cumulative incremental linear motions, in the microinch range. The proposed use of this device, was as a method of actuation for precision machining and tooling operations.

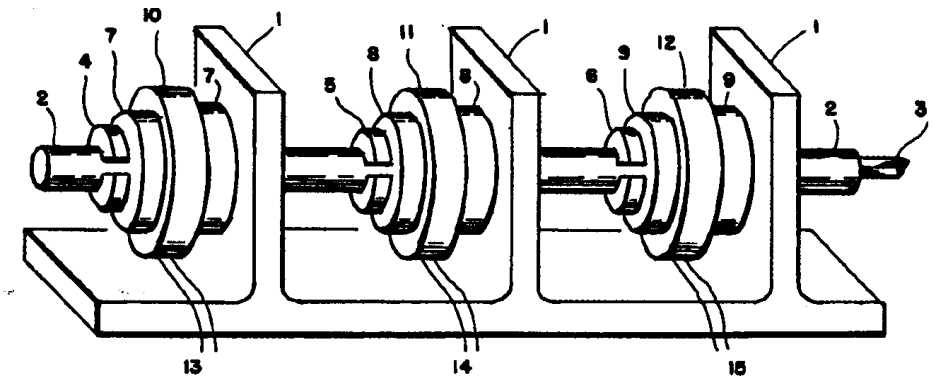

Figure 1.2: G.R. Stibitz (1964).

One of the original piezoelectric inchworm motors was introduced by S. Hsu, A. Arbor, and A. Blatter (1966). The motor made use of the hybrid "walker-pusher" technique as the method of actuation. The extending mechanism utilized a piezoelectric tube to create the forward motion. The clamping mechanisms used a one-way clamping technique, by means of two annular wedge surfaces inclined to the shaft's axis such that the wedged members could prevent motion in either direction. The direction of motion of the motor was determined by the activation of a piezoelectric disc, which in turn moves the wedged members into a position allowing motion in one direction. The device was able to produce

an unloaded velocity of 6.3 millimeters per second(mm/sec) at 60 cycles per second(Hz) and approximately 38 mm/sec at 400 Hz.

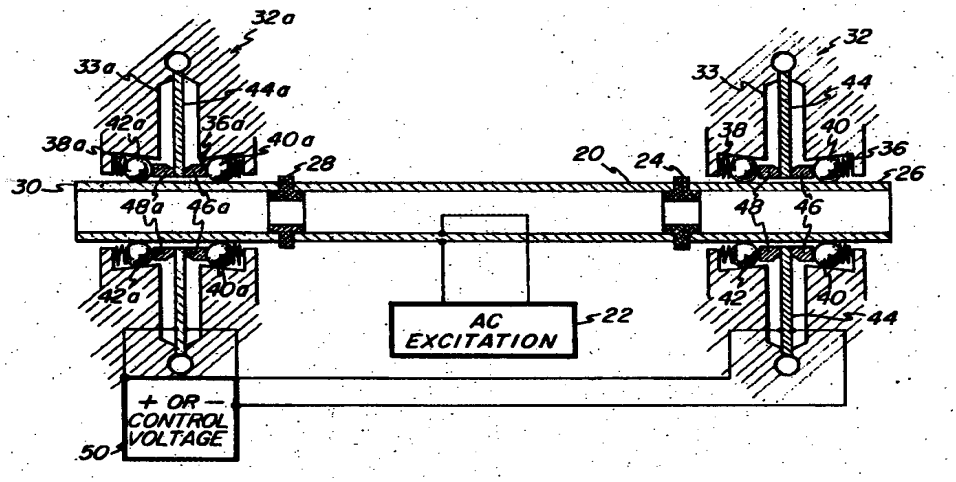

Figure 1.3: S. Hsu, A. Arbor, and A. Blatter (1966).

Another piezoelectric inchworm motor was presented by G.L. Locher (1967). This motor also made use of the hybrid "walker-pusher" technique as the method of actuation. The extending mechanism used was a piezoelectric actuator that had been directly incorporated as part of the output shaft. The clamping mechanisms are stationary mounted piezoelectric actuators that create a pinching action on the output shaft and are cycled with the extender to create forward motion. The design claims the ability to create movement with an accuracy of approximately 13 microns(um); however, its maximum travel range was limited by the design.

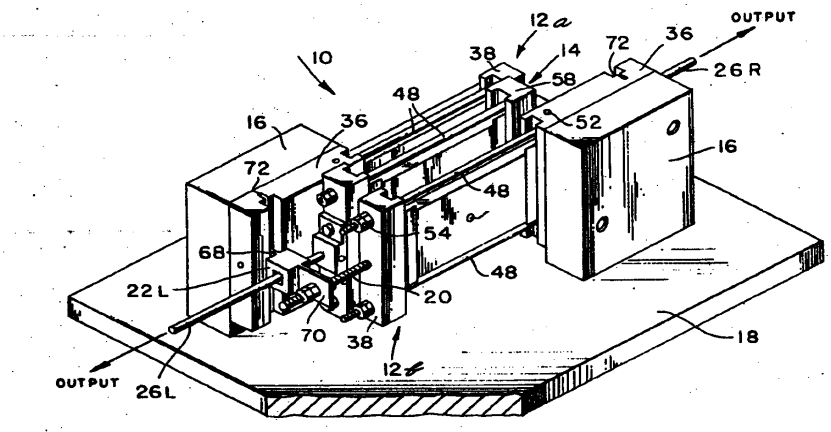

Figure 1.4: G.L. Locher (1967).

The design introduced by A.D. Brisbane (1968), is the first example of a piezoelectric "walker" motor. The extending mechanism consists of a piezoelectric tube actuator directly connected to the clamping mechanisms inside the bore of a tube. To create the clamping mechanisms, two piezoelectric disks were designed to clamp the interior of the bored tube when activated. The intent of the design was to create an actuator that can accurately position material during a machining process. The claimed result of the design, was a linear motor that had the ability to produce an increment step size down to 5 microns.

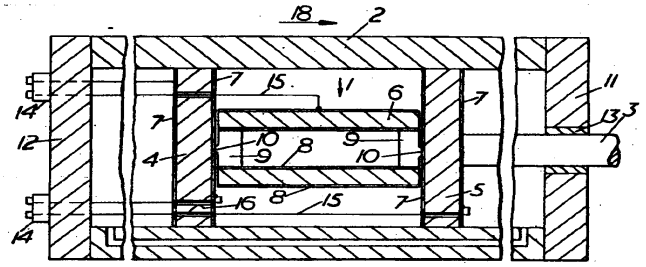

Figure 1.5: A.D. Brisbane (1968).

G.V. Galutva (1972), is the first example to use piezoelectric stacked actuators to create an inchworm type motor. The piezoelectric stacked actuators were used both to create the forward motion and to directly clamp the walls of the guide channel. The motor was designed as a "walker" with the objective to provide a device for precision displacement, in which the effect of friction on the accuracy of movement was eliminated. The design claimed to produce speeds from 0 to several hundred mm/min and also made the revolutionary claim to produce accuracy on the order of microns.

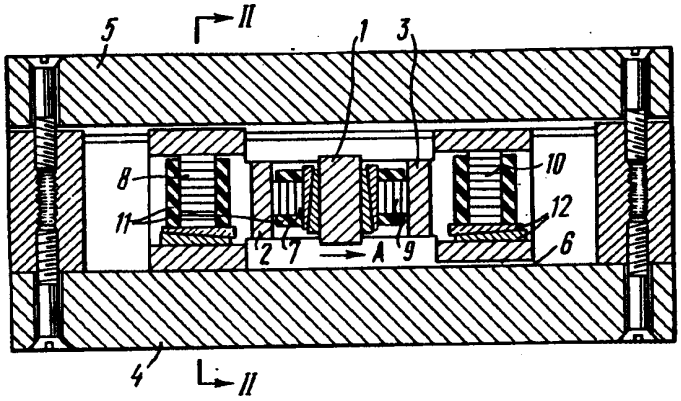

Figure 1.6: G.V. Galutva (1972).

One of the most revolutionary piezoelectric inchworm motors was introduced by R.A. Bizzigotti (1975) and W.G. May, Jr. (1975). The design created for Burliegh Instruments, Inc. was used as a basis for their production Inchworm motors. Their contribution introduced the term "Inchworm" to describe incremental linear motors. The design created was a "pusher" motor, which utilized two cylindrical PZT clamps around the outer diameter of an actuator rod with an extending PZT actuator between the clamps. As a result, the design proved to be highly accurate with a variable step size form 4 microns down to 0.004 microns.

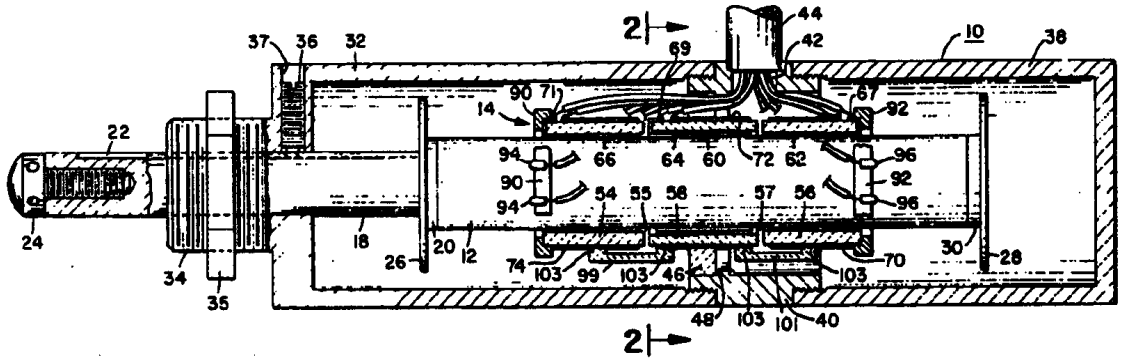

Figure 1.7: R.A. Bizzigotti (1975).

The piezoelectric inchworm motor presented by C.G. O'Neill and C.E. Foster (1980), introduced an actuator that has full clamping abilities when not activated. The design makes use of the walker technique of actuation inside of a hollow cylindrical body. The clamping mechanisms use two piezoelectric disks coupled with two slotted cups that are pushed against the cylinder walls until the disks are activated. The extending mechanism consists of a piezoelectric stack actuator.

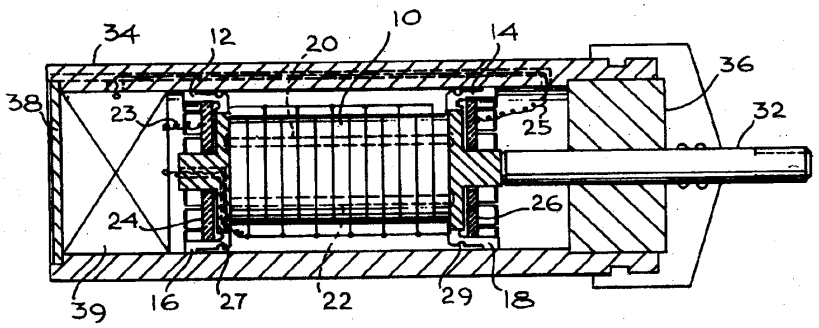

Figure 1.8: C.G. O'Neill and C.E. Foster (1980).

A device introduced by A. Hara, T. Horinchi, K. Yamada, S. Takahashi, and K. Nakamura (1986), for the most part was a copy of Bizzigotti and May's design with exception of the piezoelectric actuators used. The stacked piezoelectric actuators in this design used a greater number of layers, by reducing the thickness of each layer. The result was a motor with similar performance to Burliegh's inchworm motor with the exception that the design can operate with a voltage range from 0 to 200 volts, compared to Burliegh's 0 to 600 volts.

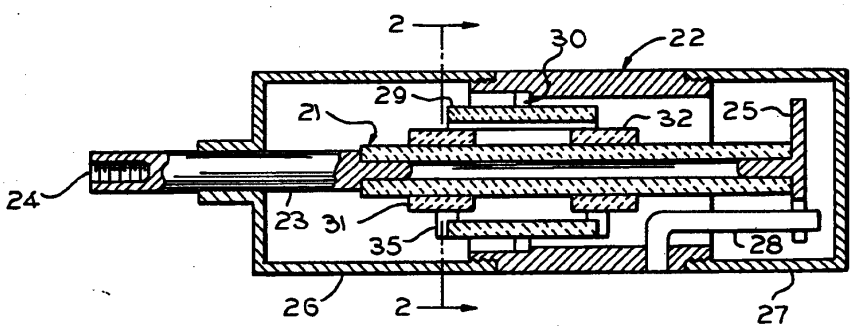

Figure 1.9: A. Hara, T. Horinchi, K. Yamada, S. Takahashi, and K. Nakamura (1986).

T. Fujimoto (1988) presented an interesting idea of using structural flexures to create a "walker" piezoelectric motor. The extending mechanism was made up of two piezoelectric stacked actuators directly coupled to the clamping mechanisms. Stacked piezoelectric actuators are also incorporated into structural flexures to create the clamping mechanisms. Granted the structural flexure can result in a loss of applied force at the walls, the displacement can be greatly amplified. This amplified displacement will allow for more flexibility of the machining tolerances. The result of the design claims to produce impressive speeds from 0 to 500 mm/sec for the unloaded case.

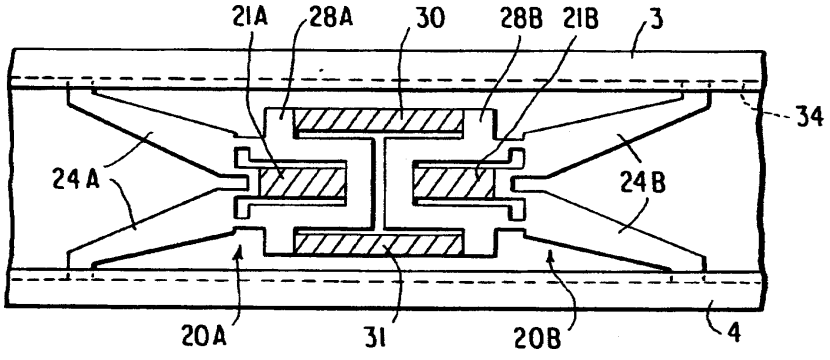

Figure 1.10: T. Fujimoto (1988).

T. Shibuya (1988) introduced an piezoelectric motor that can be categorized as either a "pusher" or "walker" motor depending on weather the shaft or the structure is held stationary. The extending mechanism of the device consists of a piezoelectric stack actuator coupled with a structural flexure that allows forward motion and maintains a preloaded compression force on the piezoelectric stack. The clamping mechanisms use a typical direct clamping action resulting from a piezoelectric stack activation. The result of the design is a rather versatile linear motor.

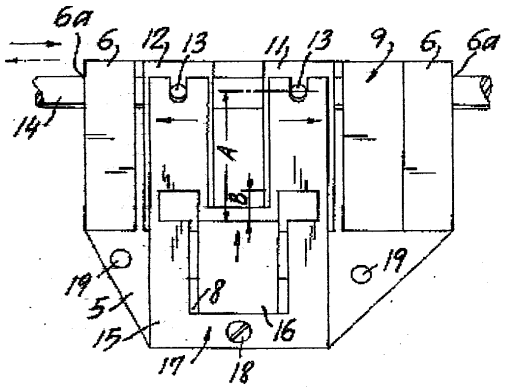

Figure 1.11: T. Shibuya (1988).

The device presented by T. Murata (1990), introduced an interesting technique of using an extremely small linear gear rack in a "pusher" type motor. The idea was to be able to engage and disengage the teeth in a method that would replace the typical frictional clamping mechanisms of most incremental motors. The method proved to be ineffective and the design was altered. However, the linear gear design would have several advantages over the typical increment motors when moving a large load.

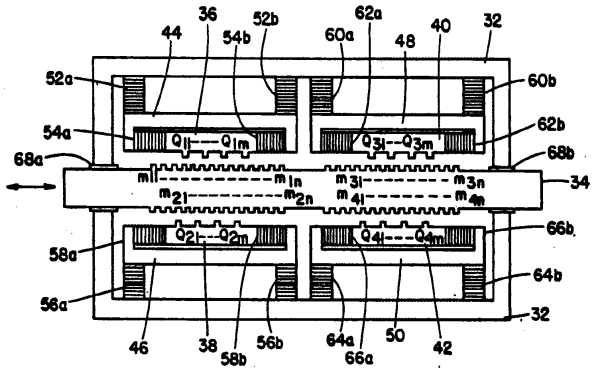

Figure 1.12: T. Murata (1990).

The linear motor introduced by J.E. Miesner and J.P. Teter (1994), represents a hybrid motor that uses piezoelectric and magnetostrictive (Terfenol-D) actuators in a "pusher" type configuration. The Terfenol-D actuators were used as the extending elements, while the piezoelectric stacked actuators were used to control the clamping elements. This design is the first example of an inchworm type motor specifically designed as high force and high speed application. The result was an unlimited travel motor able to produce a stall load of 12 kilograms(Kg) and an unloaded speed of 25 mm/sec.

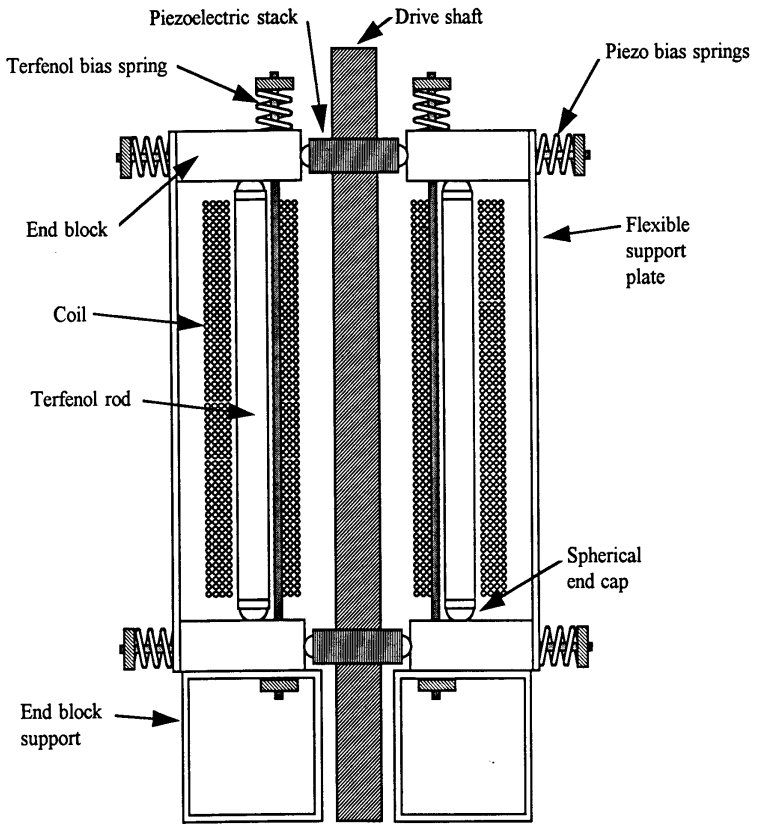

Figure 1.13: J.E. Miesner and J.P. Teter (1994).

B. Zhang and Z. Zhu (1994), introduced a incremental "walker" motor with a structure created from a single piece flexure. The flexure frame contains three piezoelectric stacks producing both the clamping and extending motions. Using the flexure frame allowed a preload to be created on the piezoelectric stacks and protected the piezoelectric stacks from shearing forces during operation. Later after further improvements Z. Zhu and B. Zhang (1997) claimed that the motor was able to produce a resolution of 5 nanometers, an output force of 200 newtons(N), and an unloaded speed of 6 mm/sec.

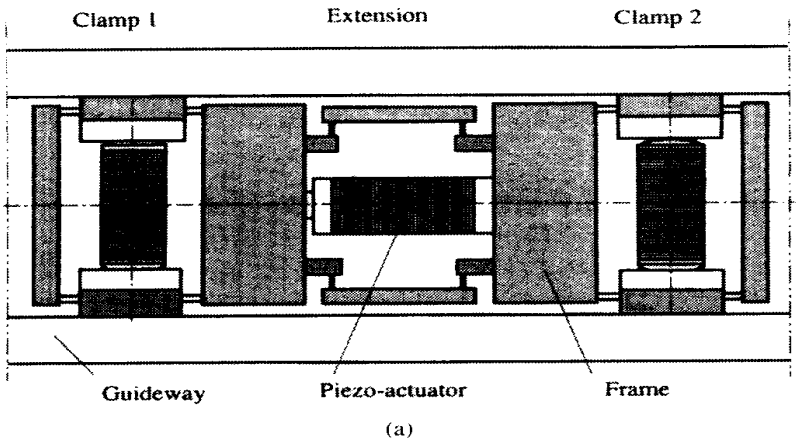

Figure 1.14: Z. Zhu and B. Zhang (1997).

A completely new idea of linear actuation based on the inchworm method was introduced by S. Lee and M. Esashi (1995). The design made use of micro-scaled etching techniques of silicon wafer material to create an electrostatic linear actuator. The resulting actuator was able to produce unloaded speeds up to 13 cm/min and a force in the millinewton range. The values are rather unimpressive until it is considered that the actuator is less than 2.5 centimeters in length.

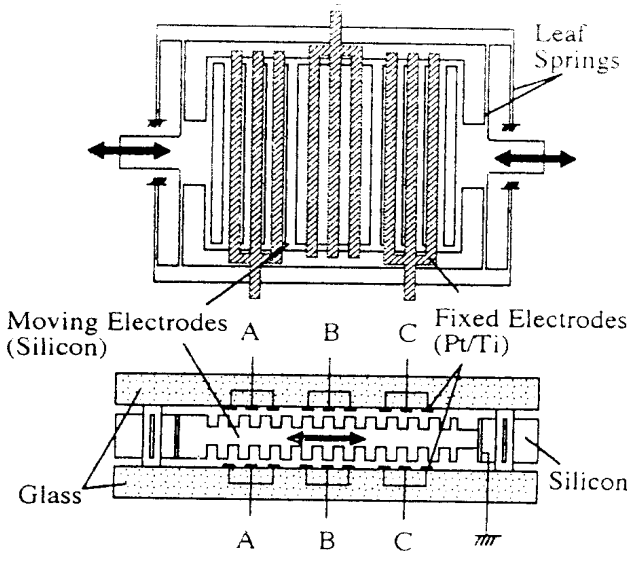

Figure 1.15: S. Lee and M. Esashi (1995).

The design presented by T. Pandell and E. Garcia (1996) was a piezoelectric caterpillar motor. The caterpillar motor used an inventive idea of using multiple clamping devices

to help reduce slipping during incremental motions. The caterpillar technique proved to be an effective design when compared to a typical inchworm motor. Results found that under loaded conditions the caterpillar motor outperformed the inchworm motor. The performance of the device claimed a stall load of approximately 20 N and an unloaded speed of 1 cm/sec; however, the improvement over the inchworm technique is the most important result of this design.

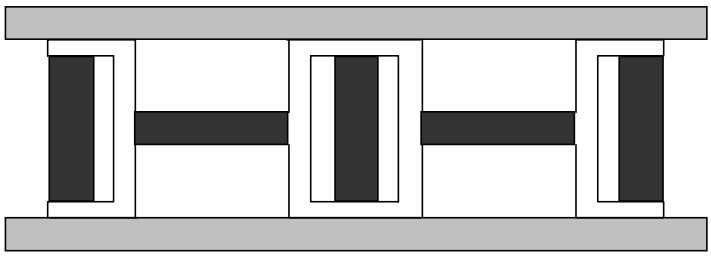

Figure 1.16: Pandell and Garcia's design.

In an effort to develop a high speed alternative to shape memory alloy based devices, Galante (1997) introduced a new method of using flexure clamps to create a "pusher-walker" piezoelectric motor. The flexure clamps in the design created a preload force on the shaft to create the maximum clamping force in the inactive state, where piezoelectric stacks were used to release the flexure clamps. However, this clamping design limited the travel range of the motor to 0.6 centimeters. The extender mechanism used a flexure design as part of the moving shaft to preload a piezoelectric stack and to allow for forward movement. The resulting motor was able to produce an unload speed of 8 mm/sec and a stall load of 40 N.

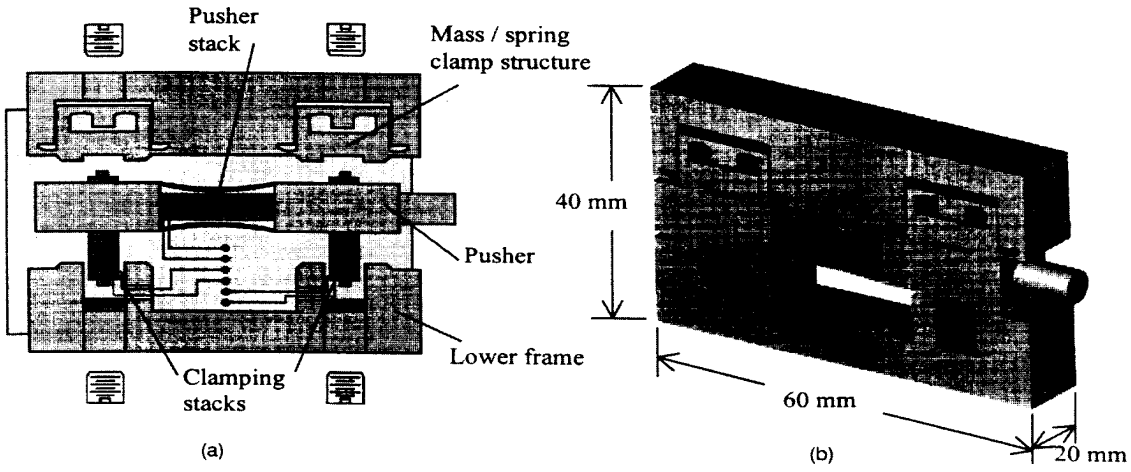

Figure 1.17: Galante (1997).

The design presented by J. Oliver, R. Neurgaoukar, J. Nelson, and C. Bertolini (1998) is another piezoelectric motor that can be categorized as either a "pusher" or "walker" motor depending on weather the shaft or the structure is held stationary. The extending mechanism of the device consists of a piezoelectric stack actuator coupled with a lever arm to amplify the stroke of the forward motion. The clamping mechanisms make use spring loaded clamping levers to apply force onto the shaft, which is counteracted by the activation of piezoelectric stacks to release the clamps. The design claims to be capable of moving large loads in the hundred pound range and can produce speed up to 125 mm/sec at approximately 500 Hz.

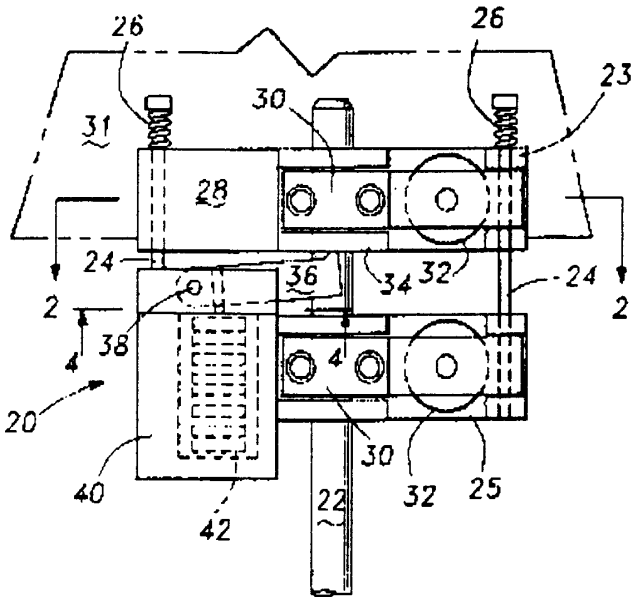

Figure 1.18: J. Oliver, R. Neurgaoukar, J. Nelson, and C. Bertolini (1998).

Similar to the designs introduced by T. Murata (1990) and S. Lee and M. Esashi (1995), G. Carman, Q. Chen, D. Yao, and C. Kim (1999) has presented a design that makes use of micro-machining techniques to create a high force, large displacement, and high precision incremental motor. The Mesoscale Actuator Device (MAD) is based on the typical inchworm type motors with the exception that mechanically interlocking microridges replace the traditional frictional clamping mechanisms. These interlocking microridges have been produced from single crystal silicon and are designed to withstand large loads. Results have shown that a pair of 5 by 5 millimeter microridged chips can supports loads up to 500 N and the motor can produce unloaded speeds up to 5 mm/sec.

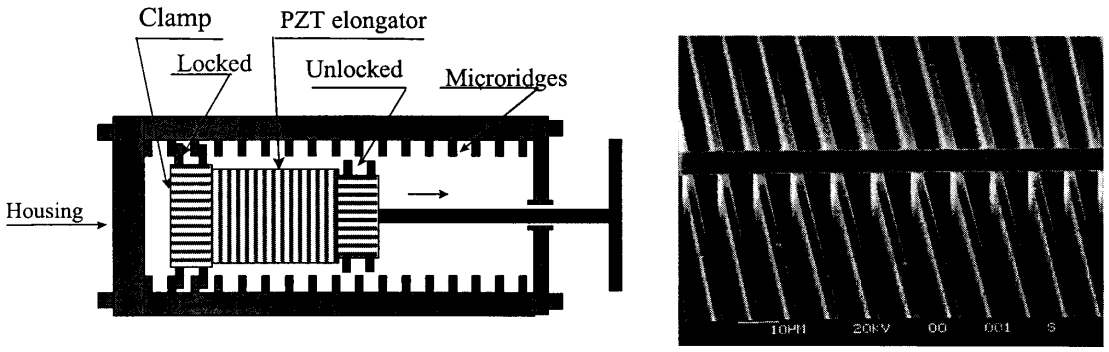

Figure 1.19: G. Carman, Q. Chen, D. Yao, and C. Kim (1999).

S. Canfield, B. Edinger, M. Frecker, and G. Koopmann (1999) has introduced an innovating "walker" piezoelectric incremental actuator for the use in minimally invasive surgery (MIS). The design incorporates the piezoelectric actuator shown in Figure 1.20 with an additional flexure structure to produce a small gripping device to be used in MIS. The actuator has been designed to run inside of a tube. The clamping mechanism employs a flexure that binds to walls of the tube when a piezoelectric stack is activated. The extending mechanism makes use of a piezoelectric stack to directly couple the two clamping mechanisms. For the gripper device to work properly the piezoelectric actuator needs to produce an actuation force of 10 newtons and a travel range of 0.31 millimeters. The design presented was able to fit inside of a tube with a 0.8 centimeter outside diameter and had an overall length of 6 centimeters, including the gripping flexure. The model created to simulate the motor predicted an actuator speed of 90 mm/sec at 1000 Hz [B. Edinger, M. Frecker, and J. Gardner (1999)].

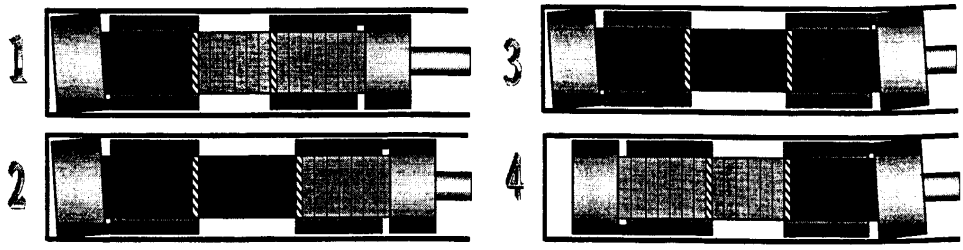

Figure 1.20: S. Canfield, B. Edinger, M. Frecker, and G. Koopmann (1999).

The last design to be reviewed, introduced by J. Frank, G. Koopmann, W. Chen, and G. Lesieutre (1999), was a "pusher" piezoelectric inchworm type actuator. The motor was

developed for applications in adaptive and conformable structures for flow control. Similar to Galante (1997) and J. Oliver, R. Neurgaoukar, J. Nelson, and C. Bertolini (1998), the clamping mechanisms made use of a design in which a spring applied the clamping force until a piezoelectric stack counteracted the force releasing the shaft. Thus, the clamping mechanisms have maximum clamping capabilities during the inactive state. The extending mechanism employed two parallel piezoelectric stacks to create the incremental forward movement. The resulting motor produced a static holding force of 350 newtons, a dynamic force of 150 newtons, unlimited travel range and unloaded speeds of 1.5 mm/sec.

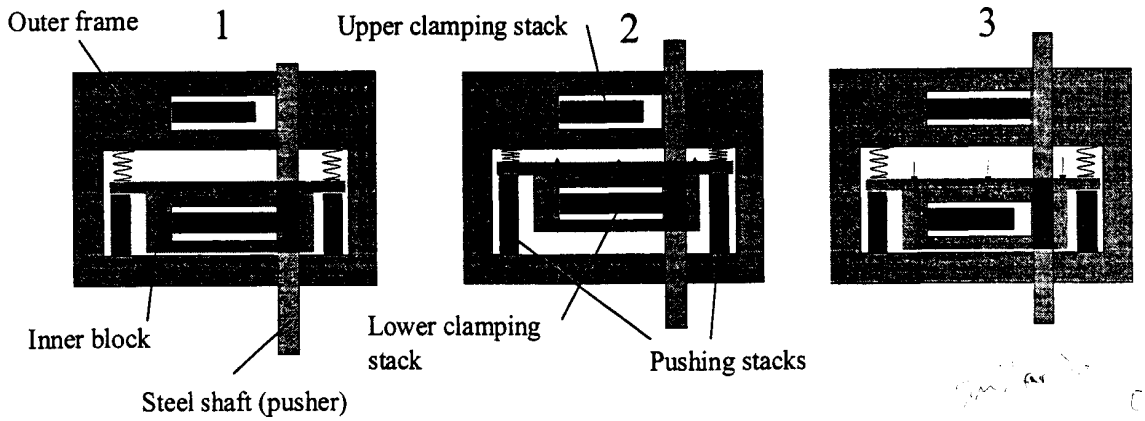

Figure 1.21: J. Frank, G. Koopmann, W. Chen, and G. Lesieutre (1999).

1.4 Overview of Thesis

1.4.1 Research Objectives

The literature survey has shown that in the past many incremental linear motor designs have focused on micro-scaled positioning to be used in industries such as precision machining and fiber optics. Departing from this trend, the research presented in this thesis will focus on designing a high load, high speed incremental linear motor with a large displacement range. The intent of the research was to design, fabricate, and test an incremental linear motor to replace the current means of linear motion. Currently, the design makes use of a DC rotary motor coupled with a linear mechanism to create the linear motion. However, the packaging of the DC rotary motor along with its linear mechanism has become an inconvenience. To alleviate the packaging concerns, it was felt that the design versatility

of an incremental linear motor could produce a design to perform the DC motor's current task, while improving the ability to package the motor.

The phase one of the project will be presented in this thesis. Phase one of the project was limited by time constraints to design and fabricate a working linear motor. Therefore, a relatively simple and low risk design was chosen to be produced and tested. The knowledge gained from the performance of the phase one motor will be used to improve upon the design and lead to a future phase two design. The desired objectives of the phase two design are to produce a incremental linear motor with the capability to move loads up to one hundred pounds and to create unloaded speeds well over 1 inch per second. Possible phase two ideas and designs will be presented later in the thesis.

1.4.2 Contributions

The project presented in this paper makes the following contributions:

- A design of an incremental linear motor in which the clamping mechanisms make use of PZT stacks preloaded using shape memory alloy wires.
- A design of an incremental linear motor in which the extending mechanism makes use a compliant amplified PZT actuator.
- A model of an incremental linear motor that makes use of a compliant amplified PZT actuator.

1.4.3 Approach

Chapter 2 is an overview of the process used to design the phase one motor. This chapter provides an introduction to the inchworm technique of actuation used to create the linear motor. The selection of a specific design for the phase one motor is then discussed, as well as the design process used to create both the clamping mechanisms and the extending mechanism.

Chapter 3 introduces the lumped parameter model used to simulate the incremental linear motor. The formulation of the model using a mass-spring-damping system to represent the designed motor is discussed. The results of this model to ideal parameters has been presented and discussed.

Chapter 4 is devoted an discussion of the experimental results and the verification of the model simulation. The similarities and differences between the experimental and model results are presented. The differences presented are analyzed and possible explanations discussed.

Finally, *Chapter* 5 summarizes conclusions of the phase one work, and proposes future work that could lead to a phase two design.

Chapter 2

Design and Fabrication of Motor

2.1 Introduction

Historically, the majority of piezoelectric inchworm motors have been designed as precise positioning devices. These micro-positioning devices take advantage of the piezoceramic characteristic to produce micron-sized displacements. For this project, the piezoceramic characteristic to produce large forces (on the order of several thousand newtons) has been exploited. The idea was to create an incremental device that can move a load forward or backward and can hold the load at any given point along a guide channel.

As mentioned previously, the focus of the design was a high force, high speed linear motor with a large displacement range. By choosing to use piezoceramic materials it was felt that the high force and high speed goals could be achieved by taking advantage of the natural characteristic of piezoceramics to produce large forces with fast response times. However, using piezoceramic materials severely limited the displacement the motor could produce. Therefore, it was decided to take advantage of an inchworm technique of motion to create large displacements.

2.1.1 Inchworm Technique

The inchworm technique is based on the simple concept of incrementally summing the relatively small displacements produced by piezoceramic elements to generate large displacements. As shown in Figure 2.1, a typical inchworm type linear motor has three major components, two clamping mechanisms (referred to as Brake A and Brake B) and an ex-

tending mechanism. During the greater part of a typical inchworm cycle, only one clamping device is to be activated at a time, this allows the extender to extend and retract freely. The clamping mechanisms are normally designed for the purpose of creating a frictional force that can withstand static forces produced by a constant load and dynamic forces produced by the extending mechanism. The purpose of the extending mechanism is to generate the small displacements in which the inchworm technique sums to produce a large displacement.

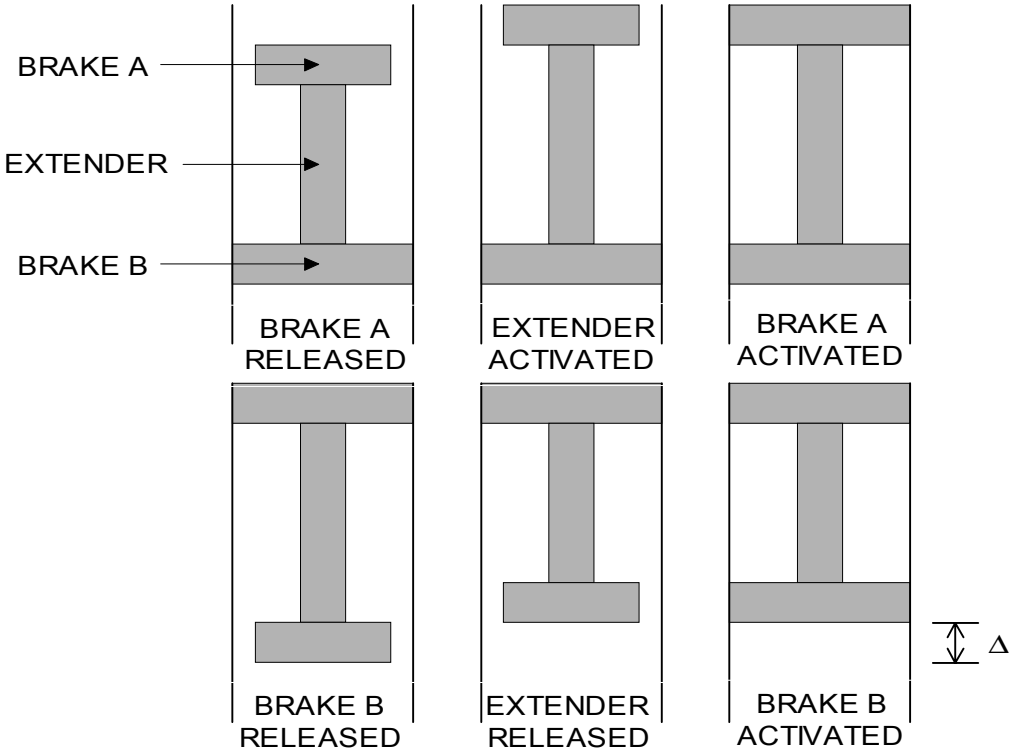

Figure 2.1: Schematic of inchworm concept.

Figure 2.1 demonstrates one full cycle of a typical incremental motor in the forward direction. At the beginning of the motion, both brakes (Brake A and Brake B) are clamped and no signal has been sent to the extender mechanism. This scenario describes a stopped motor that could possibility be holding a load stationary. The first step shown in Figure 2.1 represents the release of Brake A. Releasing Brake A frees the extender to allow motion in forward direction. In the second step the extender is activated producing a forward motion of Brake A to a new position. In the third step Brake A is activated, clamping Brake A in the new position. The fourth step shows the release of Brake B, again to allow motion of the extender in the forward direction. In the fifth step the extender is de-activated, moving

Brake B into a new position. In the last step of the cycle, Brake B is activated, clamping Brake B in the new forward position. The cycle is then repeated to create forward motion. The last step of the cycle also represents the state of each component when the motor is stationary state.

The typical cycle of a linear motor using the inchworm technique reveals that the velocity of the motor is directly dependent on the step size of the motor and the rate in which the cycle repeats. For the ideal case the velocity of the motor can be calculated as the product of the step size (Δ) and the drive frequency (f), as shown in Equation 2.1.

$$Vel = \Delta \cdot f \tag{2.1}$$

2.2 Selection of Design Method

As shown in the literature survey, there are many different methods in which a linear motor can be designed. To aid the decision of which design would best fit the project specifications a functional decomposition of piezoceramic linear motors was produced (Figure 2.2). As mentioned previously, most incremental linear motors can be broken down into three components, two clamping mechanisms and an extending mechanism. The extending mechanism can be designed using either a direct method or an amplified method of motion. The direct method of motion employs a piezoceramic stack, in which high forces can be produced. However, the displacement is limited to approximately 0.1% of the actuator's length.

The amplified method of motion can be produced using either a mechanical linkage or a compliant amplifier. Using the mechanical linkage method of amplification requires a piezoceramic stack coupled with mechanical linkage such as a lever arm to produce the amplified displacement (i.e. J. Oliver, R. Neurgaoukar, J. Nelson, and C. Bertolini (1998)). A compliant amplifier makes use of a compliant structure containing a piezoceramic stack, such that when the stack is activated the displacement produced is amplified. The use of the amplified method of motion will produce larger incremental displacements. However, the amplified method will result in a loss in force proportional to the amplification gain.

After reviewing the pros and cons for the extending mechanisms, the compliant amplified actuator was found to be the preferred choice for the project. Granted the direct

actuator produced more force, it was decided the amplified actuator was able to produce a sufficient amount of force for the task at hand. The deciding factor for choosing the compliant amplified actuator over using mechanical linkage amplification was the fact that there are several compliant amplified actuators on the market today. With the time constraints, purchasing the extending mechanism was the favored choice.

The clamping mechanisms can be separated into two different design methods, the internal mechanisms and the external mechanisms. External clamping mechanisms are designed to surround a guide shaft. There are two basic external mechanism designs. One design uses the activation of a piezoceramic stack to clamp the guide shaft (i.e. R.A. Bizzigotti (1975), while the other design uses the activation of a piezoceramic stack to release the clamp from the guide shaft (i.e. J. Oliver, R. Neurgaoukar, J. Nelson, and C. Bertolini (1998).

Internal clamping mechanisms are designed to clamp inside of a guide channel. There are two basic designs methods for internal clamping mechanisms. One internal clamping method uses an expanding technique, while the other method uses a mechanical technique of holding a position. The mechanical clamping technique can be described similar to a ratchet. The technique can use a passive design limited to one direction of motion or an active bi-directional design in which a piezoceramic element is used to switch the direction of the ratchet (i.e. S. Hsu, A. Arbor, and A. Blatter (1966)).

The expanding clamping mechanism makes use of the dimensional change of a piezoelectric stack when activated to either produce or counteract a frictional holding force. Similar to the extending mechanism, the expanding clamping mechanism can make use of either a direct means of actuation (i.e. G.V. Galutva (1972)) or an amplified means of actuation (i.e. T. Fujimoto (1988)).

After reviewing the pros and cons for the clamping mechanisms, an internal-direct-expanding clamping mechanism was chosen for the project. An internal clamping device was chosen such that it could easily be incorporated into a guide channel. The expanding method of clamping was chosen, since the design would be much simpler than a mechanical clamping design. A direct means of clamping actuation was chosen so that the maximum amount of frictional holding force would be produced, in an effort to reduce the possibility of the clamp slipping. The resulting design has been highlighted on Figure 2.2.

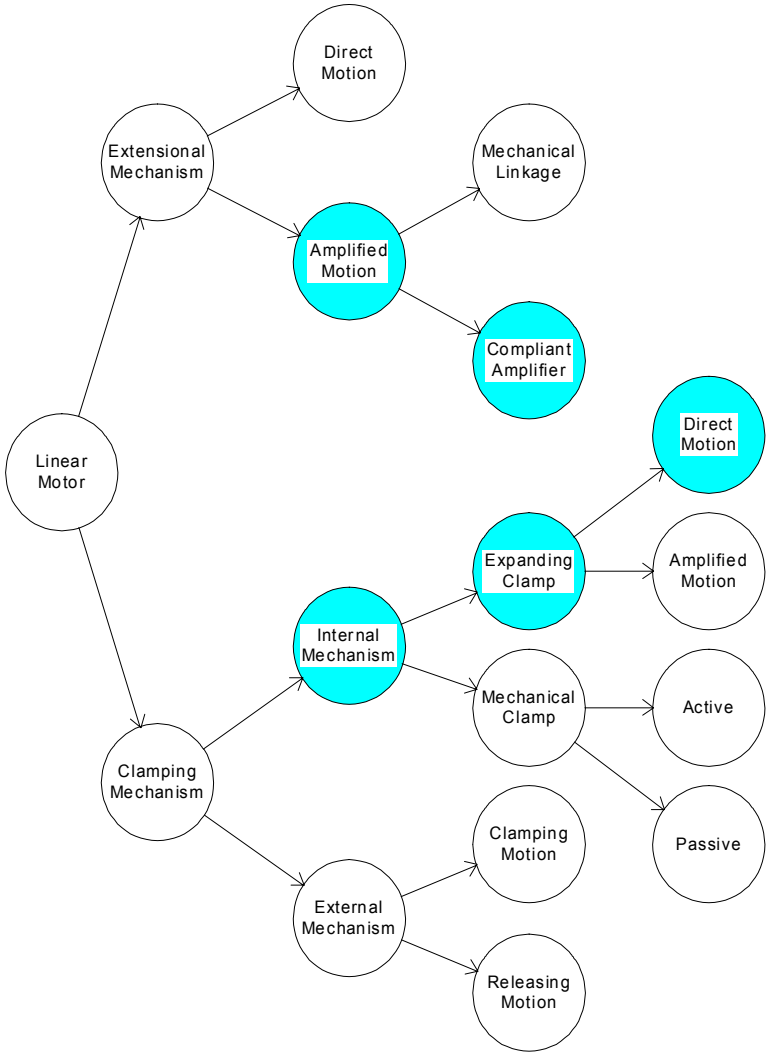

Figure 2.2: Functional decomposition of a piezoelectric linear motor.

2.3 Design and Fabrication of Extending Mechanism

As a result of the functional decomposition, the decision was made to purchase a compliant amplified actuator for the extending mechanism. Before deciding on an amplified actuator to use, a comparison was conducted to find the actuator that best suited the project. The comparison found two likely actuators that produced characteristics suitable for the project, the APA95ML and APA120ML manufactured by Cedrat Recherche. The performance characteristics for these two actuators are shown in Table 2.1.

Table 2.1: Compliant actuator characteristics [Cedrat_Recherche (2000)].

Characteristic	*Unit*	*APA95ML*	*APA120ML*
Displacement	(um)	94	120
Blocked Force	(N)	1900	1400
Stiffness	(N/um)	20.2	11.7
Voltage Range	(V)	-20 to 180	-20 to 180
Capacitance	(uF)	12.7	12.3
Height	(mm)	60	45
Length	(mm)	78.9	78.9
Width	(mm)	20	20
Mass	(g)	164	160

These two actuators were chosen for their large displacements of approximately 100 microns and high force capabilities of over a 1000 newtons. The high force capability of the actuators was sufficient for moving the loads related to the project of up to 100 pounds (445 newtons). The large displacements produced by these actuators were desired to help achieve a high speed motor. For phase one of the project, the speed of the designed motor was the primary concern. Therefore, the APA120ML amplified actuator shown in Figure 2.3 was chosen to be included as part of the design. The actuator was implemented into the design as a direct attachment between the two clamping mechanisms.

Figure 2.3: Cedrat Recherche's APA120ML.

2.4 Design and Fabrication of Clamping Mechanisms

The design of the clamping mechanisms entailed four major design obstacles:

1. The selection of actuators
2. The preloading the actuators
3. The design of a clamping interface
4. The design of a housing

2.4.1 Selection of Actuators

When deciding on the actuators to be used for the design, several aspects were considered. The actuators chosen must produce enough force such that the frictional force created could resist the static force of the load and the dynamic force of the extending actuator. The maximum static force specified by the project was 445 newtons and the maximum dynamic force produced by the extending mechanism was specified at 1400 newtons. Therefore, the total frictional force of the clamping device needed to be greater than 1845 newtons. For a clamping interface of stainless steel on stainless steel gave an ideal friction coefficient of 0.8 [Oberg and Ryffell (2000)]. Using this friction coefficient, an ideal actuator force of 2306 newtons was found necessary. Taking in account for a reduced friction coefficient and force losses due to dimensional tolerances, an actuator producing 3500 newtons was chosen. The characteristics of the chosen PZT stack type actuators purchased from Piezomechanik are shown in Table 2.2.

Table 2.2: PZT stack characteristics [Piezomechanik (2000)].

Characteristic	*Unit*	*PSt150/7x7/20*
Displacement	(um)	20
Blocked Force	(N)	3500
Stiffness	(N/um)	120
Voltage Range	(V)	0 to 150
Capacitance	(uF)	3.6
Height	(mm)	7
Length	(mm)	7
Width	(mm)	18
Mass	(g)	8

The displacement that the clamping device can produce was also considered. As seen in Table 2.2, the maximum displacement of the actuator chosen was only 20 microns. Using a single actuator for the design would require extremely tight machining tolerances of the guide channel. To gain flexibility of the machining tolerances and to create a relatively low risk design, four actuators were employed in the clamping mechanism design. The resulting clamping mechanisms would be able to produce a maximum force of 3500 newtons and a stoke of approximately 80 microns.

2.4.2 Preload of Actuators

A preload was applied to the chosen actuators before being used in the clamping mechanism. Appling a mechanical preload to multi-layered actuators will allow stacked actuators to operate in a more effective manner. Piezoceramic stacked actuators have low tensile strength and often fail under tensile stress. To prevent failure, the preload creates a mechanical bias on the stack to compensate for any applied tensile forces. The preload also creates additional return forces to aid in the release of the clamping mechanisms.

The design to preload the clamping actuators can be seen in Figure 2.4. The design makes use of a center support that bolts directly to the extending actuator, maintaining the symmetry of the device. To end caps are used to preload the actuators to the center support, through the use of shape memory alloy wires (not shown in figure). The preload force applied was approximately 20% of the actuators blocked force of 3500 newtons. The preload applied was found to provide adequate protection from tensile forces while producing a minimal loss in displacement.

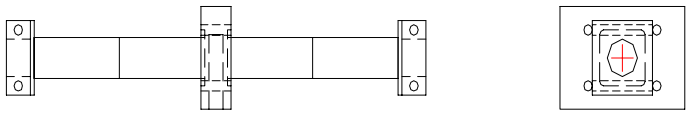

Figure 2.4: Design of actuator preload.

2.4.3 Design of a Clamping Interface

Once the preloaded actuators were designed, an adjustable interface between the preloaded actuators and the guide channel was created. The adjustable interface made use of two

cylindrical buttons directly connected to the end caps of the preloaded actuator. One button made use of a solid interface, while the other used a two part adjustable interface that could be adjusted to fit the guide channel. Once fully adjusted, the threads of the adjustable interface could be held in place by a setscrew. The adjustable interface allowed the motor to be easily placed inside the guide channel and gave some lead way on the actual dimensions of the guide channel.

2.4.4 Design of a Housing

The clamping mechanism housing then was designed, for the purposes of supporting the preloaded actuators and to prevent shear forces from damaging the stacked actuators. To support the preloaded actuator, the housing was designed such that the same screws that attached the extending mechanism also connected the center support of the preloaded actuator to the housing. To prevent shear forces from damaging the stacked actuators, two pre-impregnated bronze bushings were pressed into either end of the housing. The inside diameter of these bushings was bored and reamed to allow only enough clearance for a slide fit. The tight tolerances allowed the adjustable interface buttons to transfer shear forces to the bushings instead to the preloaded actuator. A clearance hole was also included in the housing design to allow access to the setscrew used to lock the adjustable interface. The resulting clamping mechanism housing is shown in Figure 2.5.

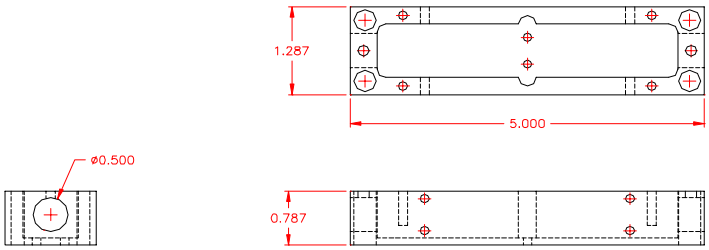

Figure 2.5: Design of clamping mechanism housing.

2.5 Design and Fabrication of Guide Channel

For phase one of the project the focus was the design of the linear motor. Therefore, the design of the channel was made rather bulky in an effort to eliminate any adverse effects the channel may have on the performance of the motor. The design of the guide channel

consisted of a four plates producing an enclosed channel. The bottom plate was important because it determined the channel's width and tolerance. For the phase one design, the width of the bottom plate was machined to +/- 0.0005 inches (+/- 13um). This tolerance was decided to be sufficient for the current clamping displacement capability of 80 microns. The two side plates were machined of stainless steel to produce the desired stainless to stainless friction coefficient at the interface. These plates were machined and polished to be bolted onto the sides of the bottom plate. The top plate bolted to the top of the two side plates and was made of lexan to provide the ability to observe the motor operating inside the channel. For the phase two design, the guide channel will most likely be ground and polished to produce the tight tolerances needed for a smaller motor.

2.6 Assembly of Motor

Figure 2.6 shows a disassembled layout of the motor. The first step in assembling the motor was to place the preloaded actuators into their housings. Then the preloaded actuators and housings were bolted to each side of the extending mechanism. The housing covers were then attached to the housing to protect the preloaded actuator. Next, the cylindrical interface buttons were placed into the housing and screwed into the end caps of preloaded actuator. A roller assembly was also designed and attached to support the motor inside the channel. For initial testing, one of the four guide rails shown in Figure 2.6 was utilized to help support and protect the extending actuator. The resulting assembled motor is shown in Figure 2.7.

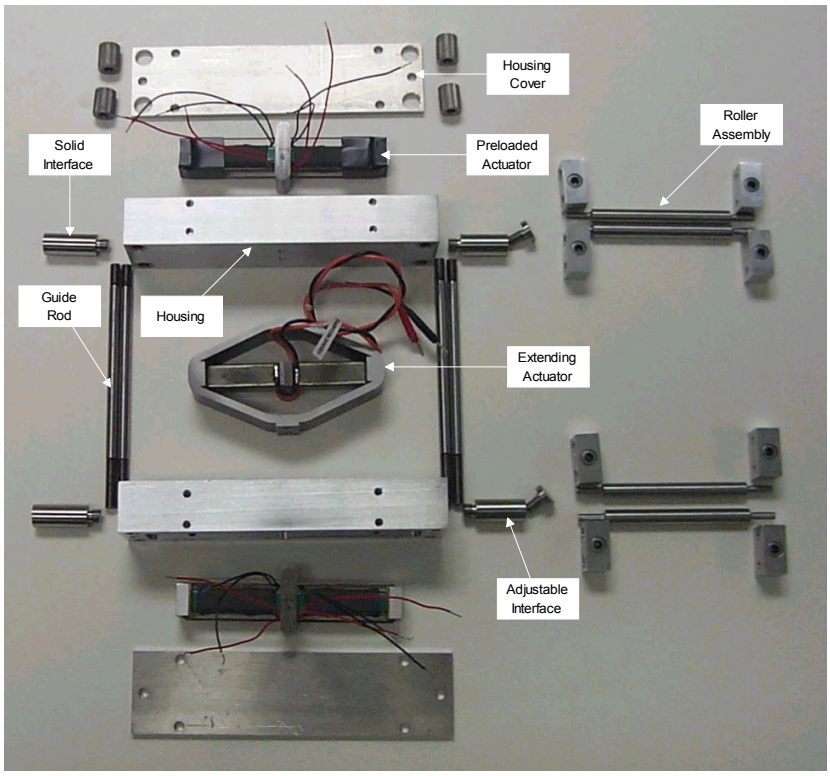

Figure 2.6: Disassembled layout of motor.

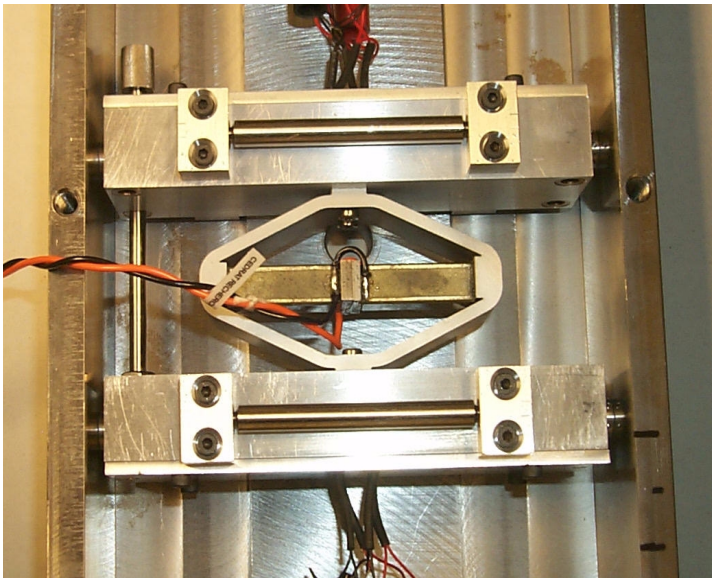

Figure 2.7: The phase one motor design.

Chapter 3

Modeling of Motor

3.1 Introduction

To predict the performance of the motor under certain conditions, a model was created using MATLAB/SIMULINK. The SIMULINK model was used to generate a dynamic simulation in which the performance of the motor could be investigated for any design parameter. Design parameters such as the input wave forms and actuator characteristics could be altered within the model to predict changes in motor performance.

3.2 Formulation of Model

To determine a model for the designed motor, one must first consider the important parameters that determine the motor's behavior. The parameters chosen to be important for the designed motor were the stiffness and damping of the extending mechanism, the mass of the clamping mechanisms, the forces applied to the motor, and the forces generated by the motor. Using these motor parameters, a two degree of freedom (2DOF) mass-spring-damper system was used to model the motor's behavior. Note that the compliant amplified actuator used in this project actually contracts when activated. Figure 3.1 shows a diagram of the chosen model

where,

$M1$ = mass of Brake 1

$M2$ = mass of Brake 2

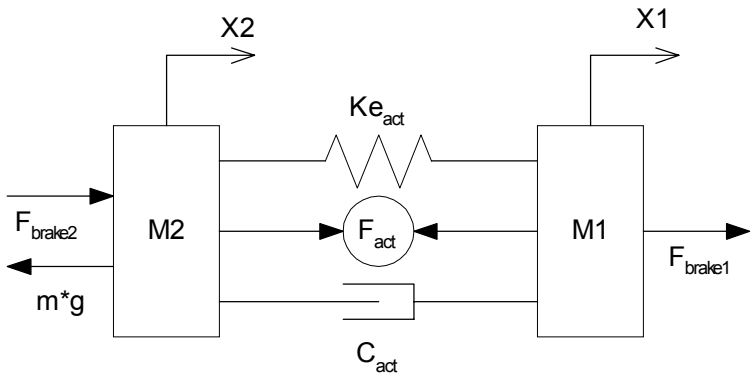

Figure 3.1: 2DOF model of motor.

$X1$ = displacement of Brake 1

$X2$ = displacement of Brake 2

Ke_{act} = stiffness of extending actuator

C_{act} = damping coefficient of extending actuator

F_{act} = force generated by the extending actuator

F_{brake1} = frictional force of Brake 1

F_{brake2} = frictional force of Brake 2

$m \cdot g$ = force of applied load

To find the equations of motion for masses $M1$ and $M2$ a free body diagram for each mass was produced (Figure 3.2). By summing the forces shown by the free body diagram the equations of motion were produced, according to Newton's second law. The resulting equations of motion for $M1$ and $M2$ are shown in Equation 3.1 and Equation 3.2, respectively.

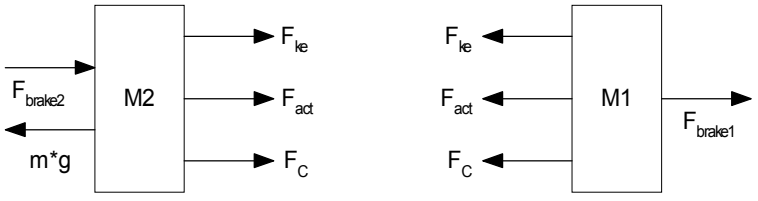

Figure 3.2: Free body diagram for $M1$ and $M2$.

$$M1\ddot{X}1 = -F_{ke} - F_C + F_{brake1} - F_{act} \tag{3.1}$$

$$M2\ddot{X}2 = F_{ke} + F_C + F_{brake2} + F_{act} - m \cdot g \tag{3.2}$$

To explain what the forces shown in the equations of motion represent, a typical force equation for piezoelectric materials must be discussed. Equation 3.3 represents the force generated by a piezoelectric material. The force generated by a piezoelectric material (F_{gen}) can be represented by the product of the mass moved (M) and the acceleration ($\ddot{X}$) in which the mass moved. The force generated is the sum of an applied force (similar to F_{act}) minus a stiffness force (similar to F_{ke}) and a force due to damping (similar to F_C). The applied force is an result to an applied voltage (V) multiplied by a voltage constant (Kv), with the units N/V. The stiffness force is calculated as the product of the actuator's stiffness (Ke) and the displacement of the actuator (X). The force due to damping is calculated as the product of the damping coefficient (C) for the actuator and the velocity ($\dot{X}$) in which the actuator is moving. All of these calculations make use of parameters that are easily found using the manufacturer's specifications.

$$F_{gen} = Kv \cdot V - Ke \cdot X - C \cdot \dot{X} \tag{3.3}$$

Applying this knowledge to the forces shown in the equations of motion (Equations 3.1 and 3.2), the following force equations are produced

$$F_{act} = Kv_{act} \cdot V \tag{3.4}$$

$$F_{ke} = Ke_{act}(X1 - X2) \tag{3.5}$$

$$F_C = C_{act}(\dot{X}1 - \dot{X}2) \tag{3.6}$$

where,

Kv_{act} = voltage coefficient (N/V) of extending actuator

$\dot{X}1$ = velocity of Brake 1

$\dot{X}2$ = velocity of Brake 2

The force generated by the brakes is similar to Equation 3.3 with two exceptions. The damping force and the stiffness force do not apply, due to the assumption that motion is prevented when the brake actuators are activated against the solid walls of the guide channel. To find the frictional forces produced by the brakes the force generated by the brakes must be multiplied by a frictional coefficient (μ). In the simulation, both a static and dynamic friction coefficient were utilized to account for brake slippage. For the frictional forces created by both Brake 1 (F_{brake1}) and Brake 2 (F_{brake2}) the same equation can be used (Equation 3.7) with the individual brake parameters applied to the equation.

$$F_{brake} = \mu(Kv_{brake} \cdot V_{brake}) \tag{3.7}$$

where,

Kv_{brake} = voltage coefficient (N/V) of individual brake actuator

V_{brake} = voltage applied to individual brake actuator

The model presented previously in Figure 3.1 provides a representation of the designed motor which makes use of the provided manufacturer specifications for both the clamping actuators and the extending actuator. However, for this project is was desired to create a more detailed model that includes a representation of the internal components of the compliant amplified actuator. This more detailed model would allow the performance of the motor to be observed for any chosen internal parameter for the compliant actuator. The ability to observe the motor's performance for different internal parameters will prove to be helpful when deciding if an amplified actuator should be designed and built to meet the project's original goals, in phase two of the project. For the more detailed model shown in Figure 3.3 the compliant amplified actuator was broken down into two components: an internal PZT stacked actuator and a compliant amplifying structure. The internal PZT stacked actuator is represented by the model as an applied force (F_{pzt}) and a stiffness of Ke_{pzt}. The model presents the compliant amplifying structure as the stiffness K_{comp} and an amplification gain ($L2/L1$).

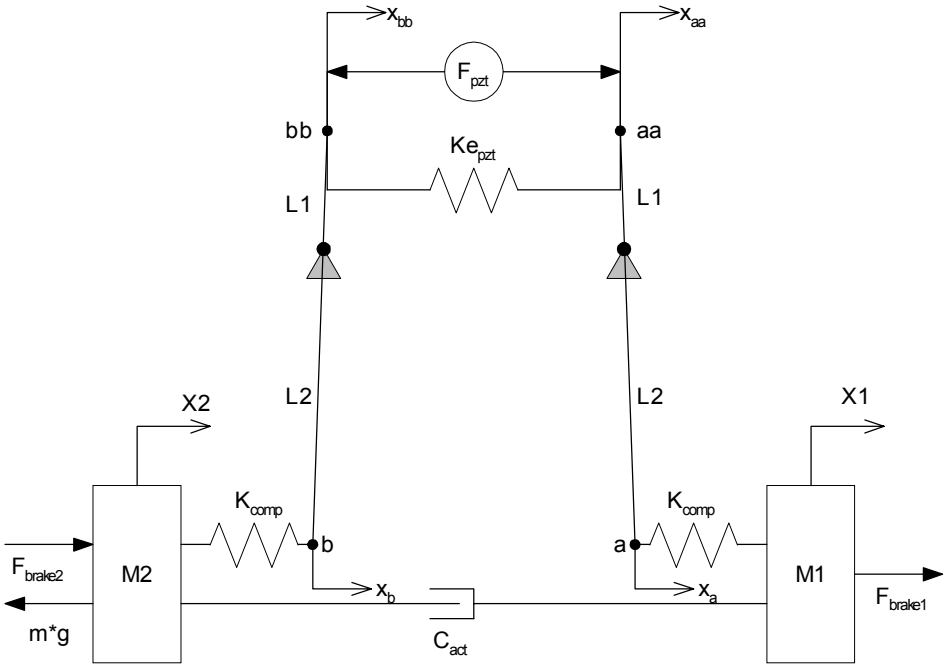

Figure 3.3: Detailed 2DOF model of motor.

where,

Ke_{pzt} = stiffness of PZT actuator used in amplified actuator

K_{comp} = stiffness of half the compliant amplifying structure

$L2/L1$ = gain of compliant structure

F_{pzt} = force generated by the PZT actuator used in the amplified actuator

Figure 3.3 can be related to the previous equations of motion (Equation 3.1 and Equation 3.2), by reducing the characteristics of the compliant amplified actuator to an equilvalent stiffness (Ke_{equ}) and an equivalent force (F_{equ}) as shown by the following equations. The equivalent force can be broken down into the product of an equivalent voltage coefficient (Kv_{equ}) and an applied voltage signal to the actuator (V_{act}).

$$M1\ddot{X}1 = -Ke_{equ}(X1 - X2) - C_{act}(\dot{X}1 - \dot{X}2) + F_{brake1} - F_{equ} \tag{3.8}$$

$$M2\ddot{X}2 = Ke_{equ}(X1 - X2) + C_{act}(\dot{X}1 - \dot{X}2) + F_{brake2} + F_{equ} - m \cdot g \tag{3.9}$$

To solve for the unknown equivalent stiffness (Ke_{equ}) and the equivalent voltage coefficient (Kv_{equ}) the model shown in Figure 3.3 was separated into six nodes: $M1$, $M2$,

a, b, aa, and bb. A free body diagram was produced for each node to find the force equation represented at each node. The following nodal equations were produced.

Node aa

$$Kv_{pzt}V_{act} - Ke_{pzt}\left(X_{aa} - X_{bb}\right) - F_{aa} = 0 \tag{3.10}$$

Node bb

$$F_{bb} + Ke_{pzt}\left(X_{aa} - X_{bb}\right) - Kv_{pzt}V_{act} = 0 \tag{3.11}$$

Node a

$$K_{comp}\left(X1 + \frac{L2}{L1}X_{aa}\right) - \frac{L1}{L2}F_{aa} = 0 \tag{3.12}$$

Node b

$$\frac{L1}{L2}F_{bb} - K_{comp}\left(\frac{L2}{L1}X_{bb} + X2\right) = 0 \tag{3.13}$$

Node $M1$

$$M1\ddot{X1} = -K_{comp}\left(X1 + \frac{L2}{L1}X_{aa}\right) - C_{act}\left(\dot{X1} - \dot{X2}\right) + F_{brake1} \tag{3.14}$$

Node $M2$

$$M2\ddot{X2} = -K_{comp}\left(\frac{L2}{L1}X_{bb} + X2\right) + C_{act}\left(\dot{X1} - \dot{X2}\right) + F_{brake1} - m \cdot g \tag{3.15}$$

Using the equations for nodes aa and bb, forces F_{aa} and F_{bb} were found to equal the following equations.

$$F_{aa} = Kv_{pzt}V_{act} - Ke_{pzt}\left(X_{aa} - X_{bb}\right) \tag{3.16}$$

$$F_{bb} = Kv_{pzt}V_{act} - Ke_{pzt}\left(X_{aa} - X_{bb}\right) \tag{3.17}$$

The equations for forces F_{aa} and F_{bb} were plugged into the equations for nodes a and b to solve for X_{aa} and X_{bb}. The resulting equations for X_{aa} and X_{bb} were produced.

$$X_{aa} = \frac{-L1\left(-Kv_{pzt}L1L2V_{act} + Ke_{pzt}L1^2X1 + Ke_{pzt}L1^2X2 + K_{comp}L2^2X1\right)}{L2\left(2Ke_{pzt}L1^2 + K_{comp}L2^2\right)} \tag{3.18}$$

$$X_{bb} = \frac{-L1\left(Kv_{pzt}L1L2V_{act} + Ke_{pzt}L1^2X1 + Ke_{pzt}L1^2X2 + K_{comp}L2^2X2\right)}{L2\left(2Ke_{pzt}L1^2 + K_{comp}L2^2\right)} \tag{3.19}$$

The equations for forces X_{aa} and X_{bb} were plugged into the equations for nodes $M1$ and $M2$ to solve for the equations of motion for the model. The resulting equations of motion were produced

$$M1\ddot{X}1 = -\left(\frac{K_{comp}Ke_{pzt}L1^2}{2\cdot Ke_{pzt}L1^2 + K_{comp}L2^2}\right)(X1 - X2) - C_{act}(\dot{X}1 - \dot{X}2)$$

$$+F_{brake1} - \left(\frac{K_{comp}Kv_{pzt}L1\cdot L2}{2\cdot Ke_{pzt}L1^2 + K_{comp}L2^2}\right)V_{act} \tag{3.20}$$

$$M2\ddot{X}2 = \left(\frac{K_{comp}Ke_{pzt}L1^2}{2\cdot Ke_{pzt}L1^2 + K_{comp}L2^2}\right)(X1 - X2) + C_{act}(\dot{X}1 - \dot{X}2)$$

$$+F_{brake2} + \left(\frac{K_{comp}Kv_{pzt}L1\cdot L2}{2\cdot Ke_{pzt}L1^2 + K_{comp}L2^2}\right)V_{act} - m\cdot g \tag{3.21}$$

where,

$$Ke_{equ} = \frac{K_{comp}Ke_{pzt}L1^2}{2\cdot Ke_{pzt}L1^2 + K_{comp}L2^2} \tag{3.22}$$

$$Kv_{equ} = \frac{K_{comp}Kv_{pzt}L1\cdot L2}{2\cdot Ke_{pzt}L1^2 + K_{comp}L2^2} \tag{3.23}$$

These detailed equations of motion (Equations 3.20 and 3.21) were assembled into a SIMULINK model. The SIMULINK block diagram shown in Figure 3.4 will simulate the motor's behavior for the chosen parameters and input signals. The corresponding MatLab files used to define values for the motor parameters and to determine whether Brakes 1 or 2 were stationary or slipping are shown later in the Appendix. The SIMULINK simulation parameters were chosen to make use of an ODE23t ordinary differential equation solver and a tolerance of 0.001.

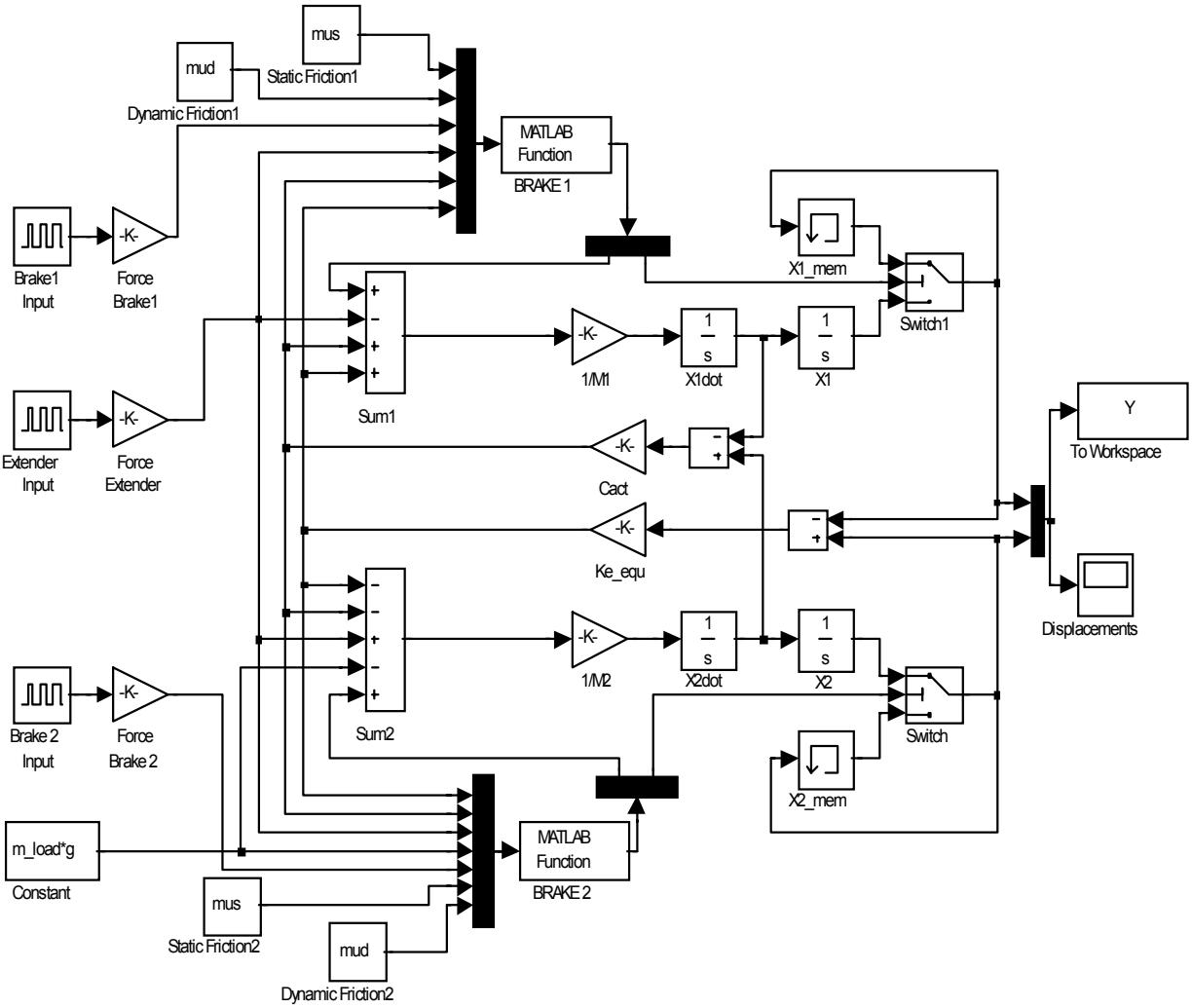

Figure 3.4: SIMULINK block diagram of modeled system.

3.3 Predicted Ideal Results

For initial simulations, the ideal parameter values used in the model were obtained from the motor design and from the manufacturer's specified actuator characteristics. Table 3.1 summarizes the parameters used for the ideal model simulation.

Before running the simulation the input voltage signals had to be chosen. The amplifiers used in the project were limited to an approximate square wave output, and also limited to a maximum run frequency of approximately 50 hertz. Above 50 hertz, saturation effects would be evident in the signals. As a result, the simulation made use of three square wave signals as inputs to the modeled system and the majority of simulations focused on

Table 3.1: Parameter values for ideal model.

Parameter	Value	Units
M1	0.471	Kg
M2	0.486	Kg
Ke_{equ}	11.67*10^6	N/m
Kv_{equ}	7.78	N/V
C_{act}	25	Kg/s
Kv_{brake}	23.33	N/V
μ_s	0.8	
μ_d	0.4	

cycle frequencies less than 50 hertz. For the two square waves used to actuate the brakes, duty cycles of approximately 60 percent were used so that one of the brakes would be activated at all times. The input waves to the brakes were phased to be nearly 180 degrees out of phase from each other, such that the combination of the three waves produced motion in a particular direction. To change the direction the motor the control signals to the brakes would be switched. Figure 3.5 shows the input control signals used for the ideal simulations. Note the activation of the extender refers to the contraction of the amplified actuator.

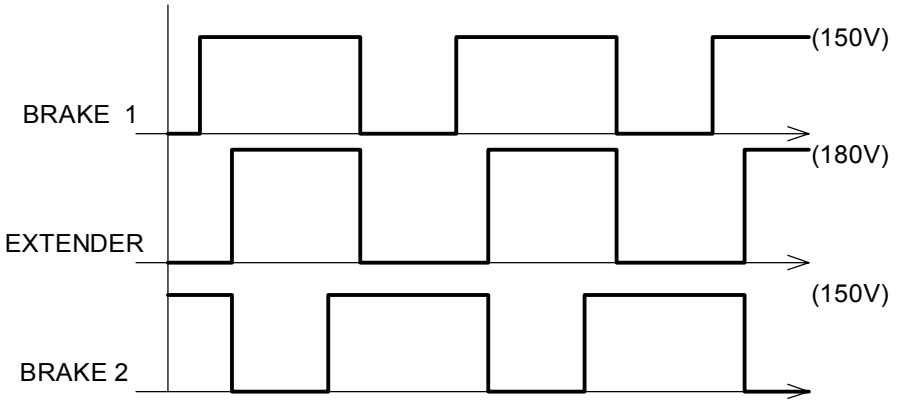

Figure 3.5: Voltage vs. Time for the ideal simulation.

A model simulation of the motor to a 10 hertz signal with no load is shown in Figure 3.6. To approximate the velocity of the motor simulation, the last displacement value produced is divided by the time it took to produce the displacement. For example, in Figure 3.6 the velocity would be equal to the displacement of 1.2 mm divided by the time of 1 second, to produce an average velocity of 1.2 mm/sec at 10 Hz. From Figure 3.6, one can also observe that the unloaded velocity of the motor will be directly proportional its

driving frequency (f) at low frequencies (Equation 3.24). Where Δ represents the step size produced by the extending actuator.

$$Vel = \Delta \cdot f \tag{3.24}$$

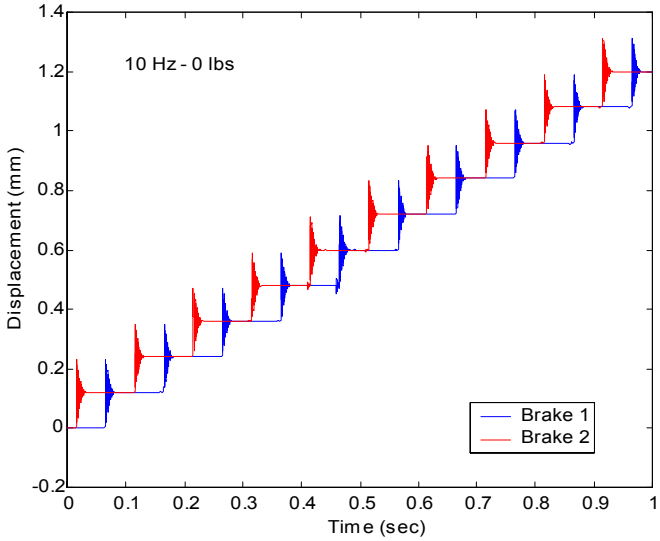

Figure 3.6: Displacement vs. Time for ideal the unloaded simulation.

However, the modeled motor is a resonant system. Therefore, the velocity of the motor will not remain proportional to frequency as the driving frequency reaches the near the resonant frequency of the motor. At these higher frequencies the step size of each cycle would change depending on the position the brake was activated during oscillation. When a load was added to the system, there were noticeable losses seen in velocity of the motor. Figure 3.7, shows close up view of the displacement verses time of the loaded motor. The point in time marked "1" represents the point in time where Brake 1 is release and the losses due to loading appear. The point in time marked "2" represents the point in time where the extending actuator is activated, producing the forward motion of Brake 1. At both the points in time the resonance of the system is evident by the oscillations that occur.

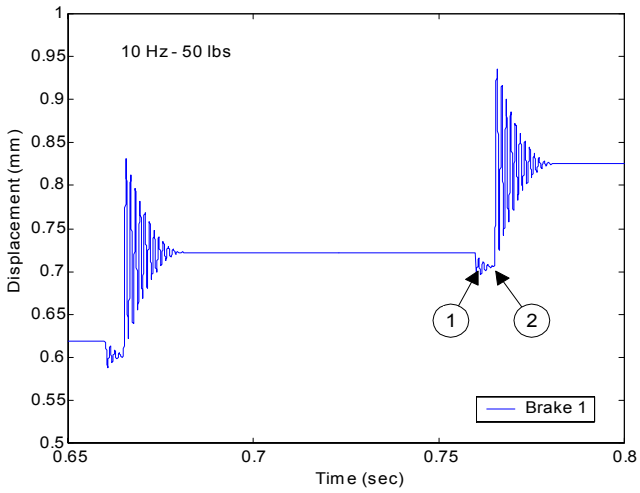

Figure 3.7: Displacement vs. Time for the ideal loaded simulation.

Figure 3.7 shows the displacement loss each cycle due to loading at the point in time "1". The displacement loss each cycle was found to equal the load applied to the motor divided by the stiffness of the extending actuator. The velocity of the ideal loaded motor can be predicted using Equation 3.25. Figure 3.8 presents the predicted velocity verses load of the modeled motor for three different driving frequencies.

$$Vel = \left(\Delta - \frac{Load}{Ke_{equ}}\right) \cdot f \tag{3.25}$$

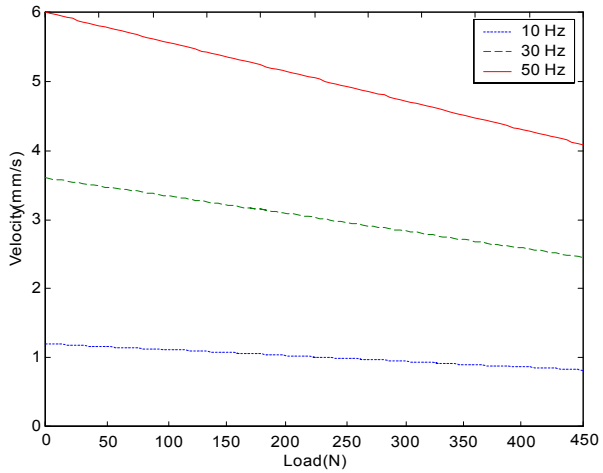

Figure 3.8: Velocity vs. Load for the ideal simulation.

The results of the ideal simulation found that the motor should produce an unloaded speed of 6 mm/sec at a drive frequency of 50 Hz. At a load of 445 newtons (100 lbs) the simulation predicted that the motor should be able to produce a speed of approximately 4 mm/sec at a drive frequency of 50 Hz. Once the frequency of the motor can be increased, the results of the simulation showed that the phase one motor should be a good step toward achieving the project's overall goals.

Chapter 4

Experimental Results and Model Verification

4.1 Introduction

This chapter provides an overview of the performance of the motor and its components. First, the actual performance of each component will be presented and compared to the expected performance. The actual performance of each component will then be used to alter the model parameters producing a corrected model. The resulting performance of the motor will then be compared to the corrected model and the differences explained.

4.2 Test Results of Clamping Mechanism

4.2.1 Stacked Actuator Testing

Before assembly of the preloaded actuators, the performance of the PZT stacked actuators was tested. The displacement of each actuator was tested to confirm the manufacturer's specifications. Using the results, the PZT stacks were placed within the preloaded actuators so that the assembled clamping mechanisms would perform symmetrically.

A diagram of the experimental setup used to test the individual PZT stacked actuators is presented in Figure 4.1. The diagram shows a PC labeled "Dspace PC", this represents a computer loaded with the hardware and software for the Dspace digital signal processor (DSP). The Dspace DSP was used throughout the project to record data and to

produce desired signals. For the testing of the stacks the Dspace PC was used to create a 2 Hz sign wave. The sine wave was sent to the Trek Linear Amplifier to produce a 2 Hz sign wave from -30 V to 150V. This signal was applied to the PZT stack actuator and the Dspace recorded the displacement measured by the Polytec OFV3001 Laser Vibrometer. The PZT stack was securely mounted to large cement column to reduce measurement error.

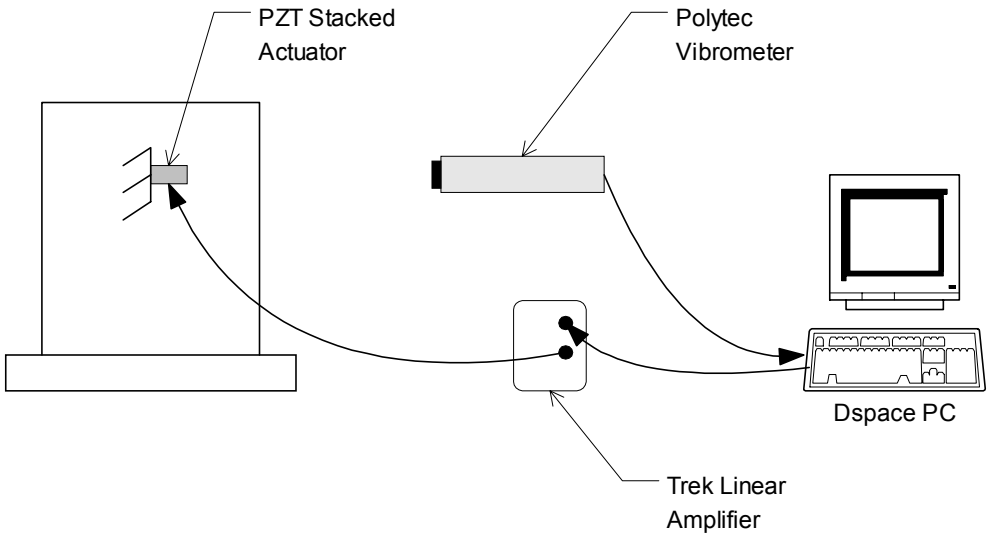

Figure 4.1: Experimental setup to test the displacement of the PZT stacks.

The performance of the PZT stacks can be demonstrated by a typical displacement verses voltage curve, shown in Figure 4.2.

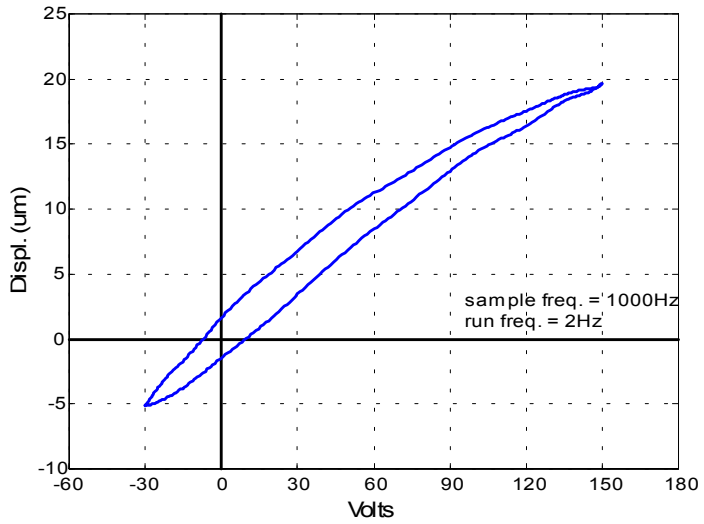

Figure 4.2: Displacement vs. Voltage for a PZT stack.

From Figure 4.2, one can observe the hysteresis that occurs naturally within PZT stacks during open-loop operation. The figure also demonstrates a nonlinear response, a typical characteristic of piezoelectric materials. More importantly the figure showed that the maximum displacement of the actuator at a voltage of 150 volts was near the specified 20 microns. A summary of the performance for each PZT stack used is shown in Table 4.1. By means of this table the position of each stack for the assembly of the preloaded actuators was chosen to maintain symmetry.

Table 4.1: Displacement comparison of the PZT stacked actuators.

Actuator	*Max Volt. (V)*	*Min Volt. (V)*	*Max Displ. (um)*	*Min Displ. (um)*	*Total (um)*
1	150	-30	19.7	-5.2	***24.9***
2	150	-30	21.2	-4.1	***25.3***
3	150	-30	20.5	-4.4	***24.9***
4	150	-30	20.3	-4.6	***24.9***
5	150	-30	20.6	-4.3	***24.9***
6	150	-30	20.6	-4.6	***25.2***
7	150	-30	20.9	-4.2	***25.1***
8	150	-30	20.9	-4.2	***25.1***

4.2.2 Preloaded Actuator Testing

In order to determine the effect of preloading on the PZT stacks, displacement testing was conducted on the preloaded actuators. The experimental setup used to test the displacement of the preloaded actuators was the same as mentioned in the previous section, with the exception that each side of the preloaded actuators was tested separately. Displacement verses voltage curves similar to Figure 4.2 were produced for both preloaded actuators. The results found that preloading the PZT stacks had a minimal effect on the expected displacement. A 2 micron reduction in displacement was contributed to the preload. Table 4.2 summarizes the displacement produced by the preload actuator for both sides A and B of brakes 1 and 2. Note that there was less than a 1 micron difference between the displacements, the symmetry was maintained.

Table 4.2: Displacement comparison of preloaded actuators.

Brake	*Max Voltage (V)*	*Min Voltage (V)*	*Total Displ. (um)*
1A	150	0	***38.8***
1B	150	0	***39.3***
2A	150	0	***39.2***
2B	150	0	***39.6***

4.3 Test Results of Extending Mechanism

Similar to the actuators used for the clamping mechanisms, the performance of the extending actuator was tested. The experimental setup to test the performance of the extending actuator was similar to Figure 4.1 where the extending actuator was mounted securely to the column. The provided manufacturer specifications for the APA120ML actuator (Table 2.1) stated that the actuator would produce an approximate 120 micron displacement at a voltage of 180 volts. The test results shown in Figure 4.3 found that the actuator actually produced a 149 micron displacement for a 180 volt input. This 29 micron increase in displacement over the expected value, increased the expected motor performance under unloaded conditions. However, the increased actuator displacement was likely the result of a lower actual actuator stiffness than expected. This lower actuator stiffness would reduce the motor's performance under loaded conditions by increasing the losses which occur each cycle due to loading. Therefore, tests to approximate the actuator's stiffness would have to be conducted.

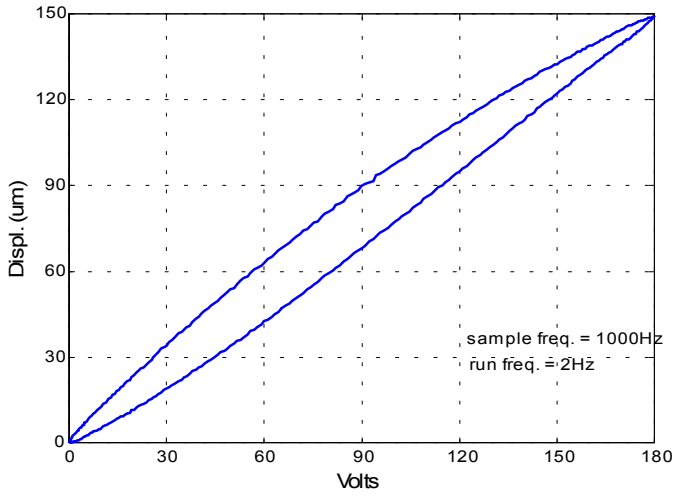

Figure 4.3: Displacement vs. Voltage for APA120ML actuator.

To test the actuator's stiffness, first a static load verses displacement test was conducted. For the test, the extending mechanism was securely mounted to the cement column shown in Figure 4.1 and several known loads up to 111 newtons (25 lbs) were applied to the actuator. The Polytec vibrometer was used to measure and record the displacement for each applied load. The test results shown in Figure 4.4 found that the stiffness of the actuator was approximately 6.78 N/um, much less than the expected value of 11.67 N/um. Since the static test only tested the stiffness of the actuator at a fraction of its maximum load capabilities (1400 N), a more accurate testing method was then preformed.

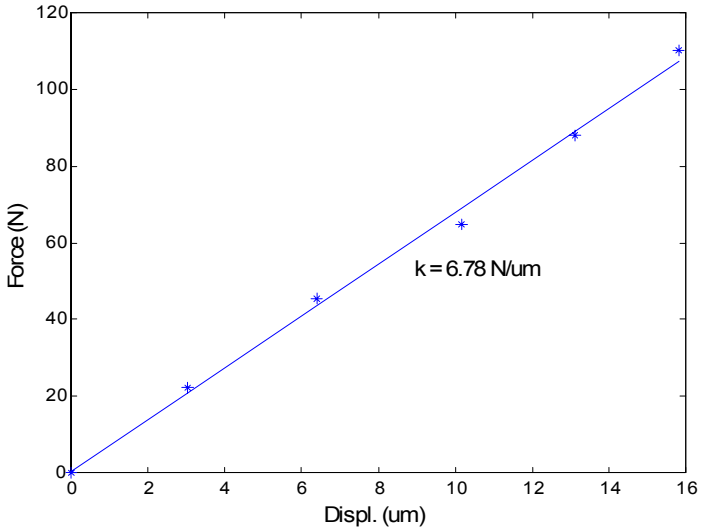

Figure 4.4: Static Load vs. Displacement for APA120ML actuator.

To obtain a more accurate stiffness measurement, a frequency response analysis was performed on the actuator. To perform the test a Tektronix 2630 Fourier Analyzer was utilized to produce the frequency response. The results of the frequency response shown in Figure 4.5 found that the actuator produced a resonant frequency at 1081 hertz. Using the resonant frequency equation for a typical spring-mass system, an equation solving for the stiffness of the actuator was found (Equation 4.1).

$$\omega_{res} = \sqrt{\frac{Ke_{equ}}{m_{act}}} \qquad \Longrightarrow \qquad Ke_{equ} = m_{act} \cdot \omega_{res}^2 \tag{4.1}$$

Appling the mass of the actuator (m_{act}) and the resonant frequency of the system in radians per second, the stiffness of the actuator (Ke_{equ}) was found to equal 7.29 N/um.

Due to the reduced stiffness of the actuator, the output force of the actuator was also reduced. To approximate the force output of the actuator Equation 4.2 was used, in which the stiffness of the actuator was multiplied by its maximum displacement (Δ).

$$F_{act} = Ke_{equ} \cdot \Delta \tag{4.2}$$

The results found that the actuator was only able to produce approximately 1094 newtons of force. A reduced performance compared to the expected 1400 newtons of force.

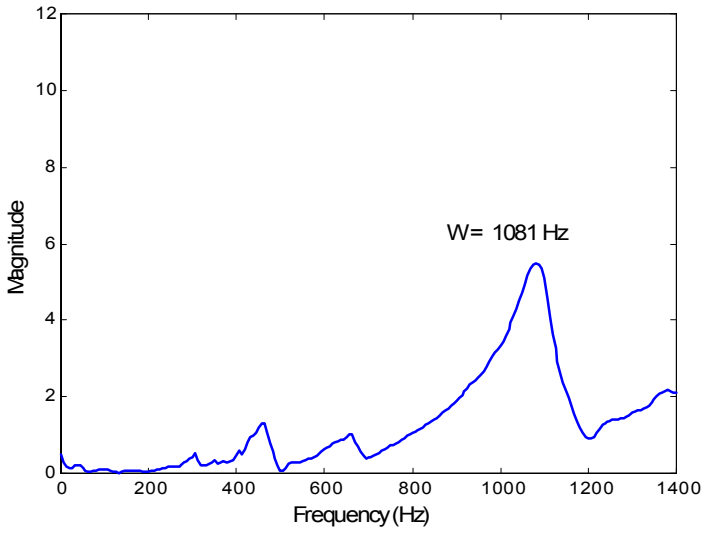

Figure 4.5: Frequency response of the APA120ML actuator.

To improve model parameters a good approximation of the actual damping coefficient (C_{act}) was found for the actuator. Using the Tektronix 2630 a time response of the actuator to an impulse input was recorded. The time response was matched to an exponential decay according to Equation 4.3. Where, x is the displacement at time t, A is a magnitude, ω_{res} is the resonant frequency, and ζ is the damping ratio. As a result a damping ratio of 4.2 % was found. Using Equation 4.4 an approximate damping coefficient of 90 Kg/sec was found for the extending actuator. The actual time response results are shown in Figure 4.6.

$$x(t) = A \exp^{-\zeta \omega_{res} t} \tag{4.3}$$

$$C_{act} = 2\zeta \sqrt{Ke_{equ} \cdot m_{act}} \tag{4.4}$$

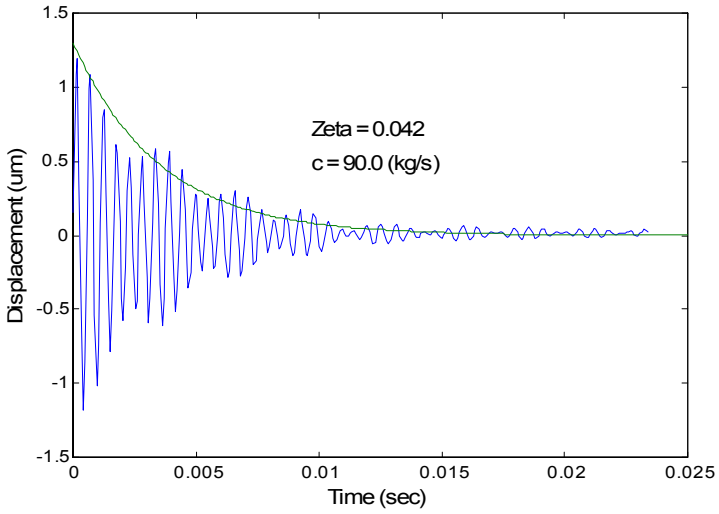

Figure 4.6: Time response of the APA120ML actuator.

4.4 Motor Performance and Model Verification

For the results presented in this section, the amplifier used to control the extender was limited to a maximum output voltage of 130 volts. The amplifier also limited the waveform input to the extender to a square wave approximation. It should be noted that the voltage limitation reduced the maximum displacement of the extender, thus reducing the velocity of the motor.

4.4.1 Experimental Setup

The setup used to test the performance of the designed motor is shown in Figure 4.7. First, the motor was placed into the guide channel and the adjustable interfaces were adjusted to minimize the clearance between the clamping interface and the guide channel. Using the Dspace DSP the desired control signals for each component of the motor were created. These signals were sent through three separate amplifiers to achieve the desired voltage signal at each of the motor's components. While the motor was running, the Dspace DSP recorded the motor's displacement as function of time from the Polytec Laser Vibrometer.

4.4.2 Unloaded Case

For the unloaded case, a comparison was conducted between the experimental and model results at a cycle rate of 10 Hz. In Figure 4.8a the comparison shows that the modeled

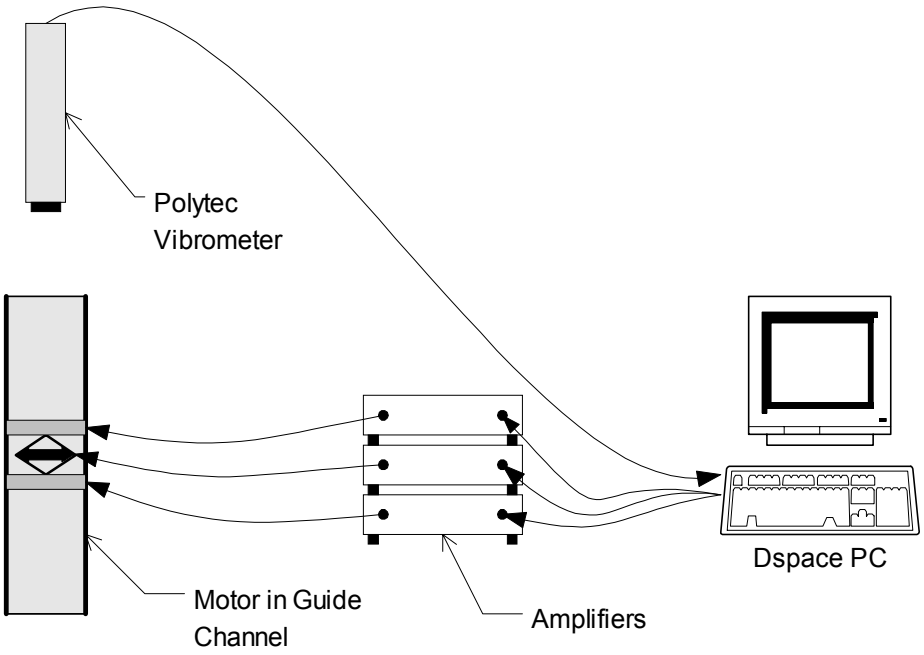

Figure 4.7: Experimental setup to run the motor.

results closely matched the experimental results. The comparison found that the modeled simulation produced a displacement of 0.3 millimeters less than the experiment over a time of 10 seconds, a difference in velocity of 0.03 mm/sec. To observe the differences between the results a cutaway view of the comparison is presented by Figure 4.8b. In the cutaway view the reason for the modeled simulation's underestimate is revealed. At low frequencies "creep" affects the experimental results by increasing the step size. "Creep" as shown in Figure 4.8b, is the small increase in displacement of an activated PZT stack as time goes on [Physik_Instrumente (1998)]. As drive frequencies increase the effect of creep on experimental results will be less evident.

From observing the cutaway view, one can also notice that the experimental results demonstrated much more damping than the modeled simulation. One reason for the difference can be attributed to the input signal to the extender. The input square wave approximation produced by the amplifier was similar to a true square wave with the activation and deactivation slopes comparable to the first half of a sine wave and the later half of a sine wave, respectively. Therefore, the input signal gives the appearance of a damped response. Another reason for the difference, was the increased damping due the friction between the guide channel and clamping interface during forward movement. For phase

one the project this difference in damping did not drastically affect the modeled simulation, so the modeled damping was left equal to the damping of the extending actuator (C_{act}).

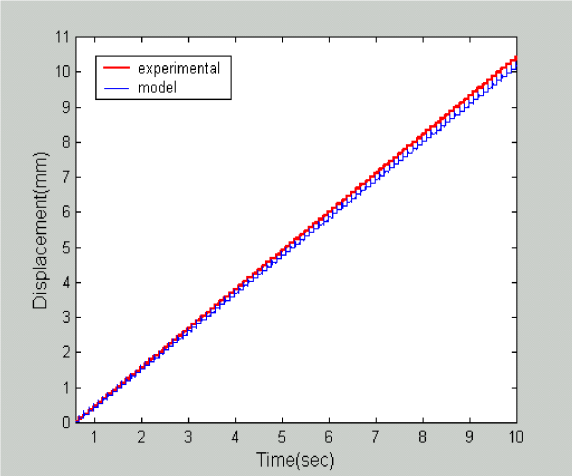

Figure 4.8a: Experimental to model comparison for an unloaded motor.

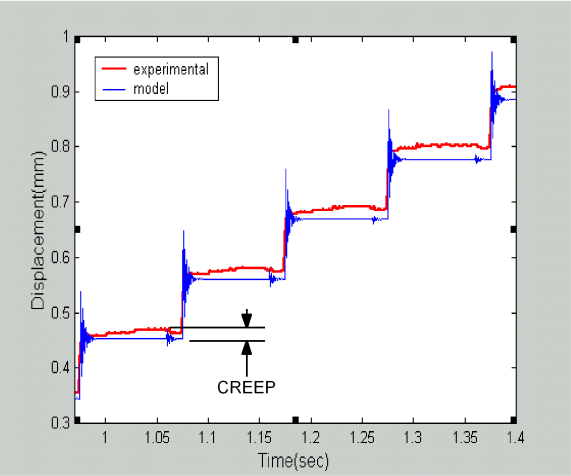

Figure 4.8b: Cutaway view of comparison.

The resulting performance of the linear motor for an unloaded case found that a speed of 4.9 mm/sec could be produced for a max voltage input of 130 volts at 50 Hz. The model slightly overestimated the result to be 5.4 mm/sec. A summary of the unloaded results is shown in Figure 4.9. Using the model the predicted performance of the motor using the full voltage input to the extender (180 V) at 50 Hz was found to equal 7.5 mm/sec.

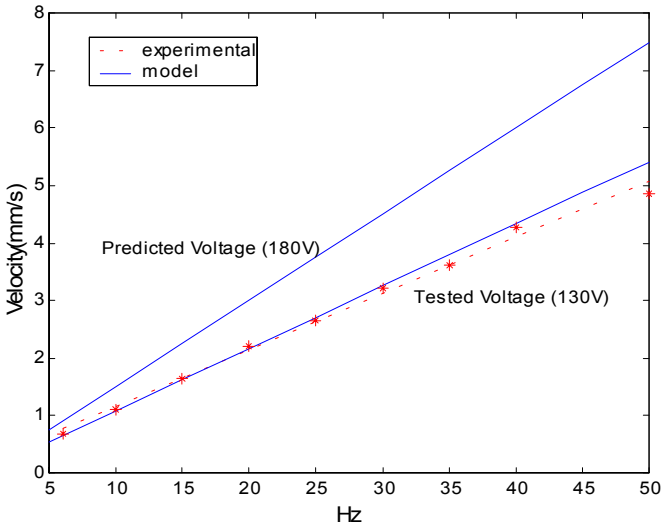

Figure 4.9: Velocity vs. Frequency for designed motor.

4.4.3 Loaded Case

For the loaded case, a comparison was conducted between the experimental and model results of moving a 9.1 kilogram (20 lbs) load at a cycle rate of 10 Hz. In Figure 4.10a the comparison shows that model simulation did not closely predict the experimental results. The model simulation predicted the motor would move 6.7 mm in seven seconds, when in actuality the motor moved 5.2 mm in seven seconds. An average loss of approximately 21 microns per cycle was unaccounted for by the model. To better understand what caused these additional losses a closer look was taken at the experimental results.

A closer look at the experimental results found both consistent and inconsistent losses. To help explain the losses a summary of typical loaded cycles is shown in Figure 4.10b. The inconsistent losses occurred at the points in time 2 and 3. At point 2 the inconsistent loss occurred when Brake 1 was activated and Brake 2 was deactivated. The loss produced was assumed to be a result of the clearances between the cylindrical button interfaces and their supporting bushings of Brake 1. For point 3 the losses occurred when the extender was activated pulling Brake 2 and the load forward. Initially it was felt that the losses at this point was due to slipping at the interfaces. However, the fact that losses at point 2 and 3 were never seen in the same cycle lead to a different conclusion. The conclusion found that when a loss did not occur at point 2 due to button interface clearances, occasionally at point 3 the loss due to button interface clearances would appear. Neither the loss at point 2 or at point 3 was guaranteed to occur during every cycle. However, the frequency in which the losses occurred increased with load. Due to the unpredictability of these losses it was difficult to accurately model the losses. Therefore, in phase one of the project the inconsistent losses were not included in the model. At point 3 consistent losses occurred when Brake 2 was activated and Brake 1 was deactivated. The model takes in account the losses due to a loaded/unloaded condition at this point; however, additional losses were found evident. These additional losses were assumed to be a result of the clearances between the cylindrical button interfaces and their supporting bushings of Brake 2. The consistency of the losses at point 3 allowed the losses to be included in the model simulation.

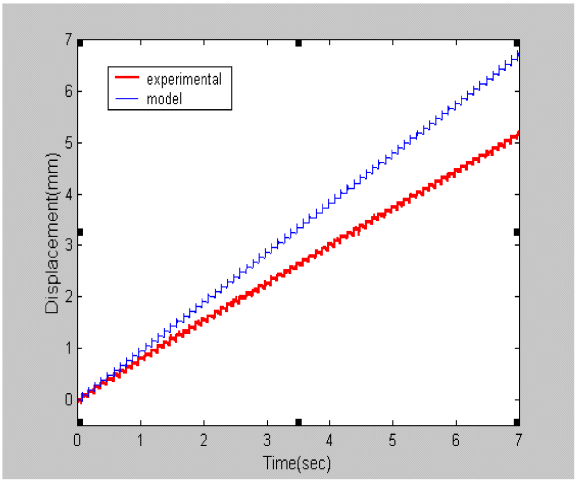

Figure 4.10a: Experimental to model comparison for the loaded motor.

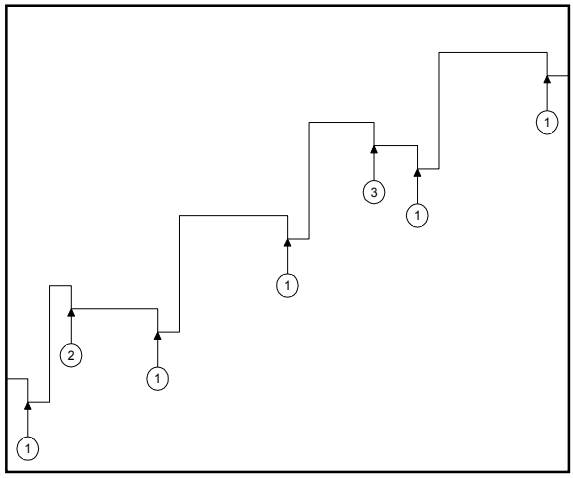

Figure 4.10b: Losses due to loading.

To improve the performance predicted by the model, the stiffness of the compliant structure was reduced to match the consistent losses. The fact that the consistent losses appeared at the same time as the loading losses, allowed a reduction in stiffness of the compliant structure to match the experimental results. By reducing the compliant structure stiffness the possible step size produced by the actuator will be maintained. However, the force produced by the actuator will be reduced and the rise time will be increased. Since phase one of the project only looks at low frequencies (below 50 Hz), this reduction in stiffness will work well. To predict the motor's loaded performance at higher frequencies the method used to account for the consistent losses will have to be changed. Using the improved model the comparison between the model simulation and experimental was produced again (Figure 4.11a). The improved model simulation predicted the motor would move 5.5 mm in seven seconds, when in actuality the motor moved 5.2 mm in seven seconds. A result was an improved average of unaccounted losses from approximately 21 microns to 4 microns per cycle. The model simulation still over estimated the experimental results due to the erratic losses, but produced relatively similar results for small loads, less that 9.1 Kg (20 Lbs).

To summarize the results for the loaded case a velocity verses load plot is shown in Figure 4.11b. Ideally the model simulation shows that the loss in velocity due to loading should have a linear relationship. In actuality the rate of the loss in velocity increased as the loading increased. This was an immediate result of the regularity in the erratic losses increasing as the load increased. The experimental results of the loaded case were

extrapolated to find that the phase one design has a stall load of approximately 17 kilograms (38 lbs).

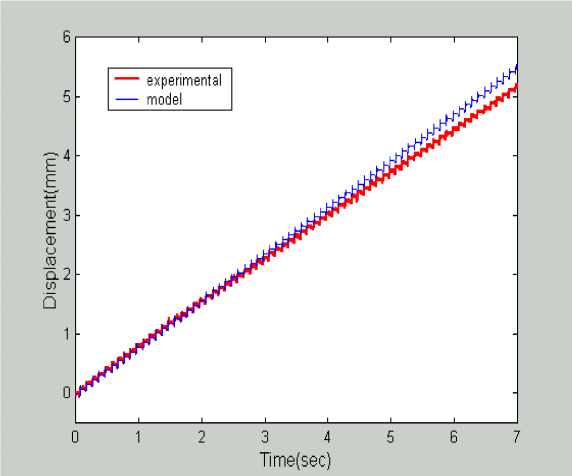

Figure 4.11a: Experimental to improved model comparison.

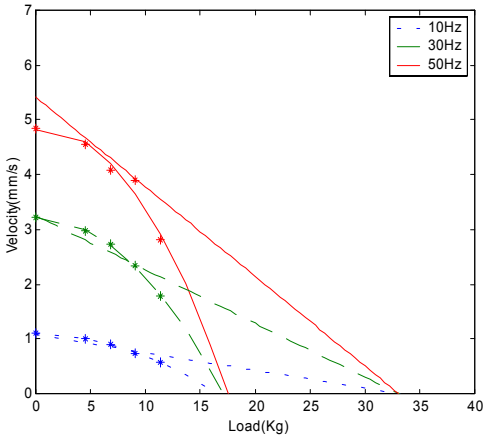

Figure 4.11b: Speed vs. Load for designed motor.

4.4.4 Power Characteristics

To create a more efficient phase two motor, the power characteristics of the phase one motor were investigated. The mechanical power output of the motor as a function of load was examined to find the operating conditions that produced the peak motor performance. The power necessary the drive the motor was assessed to find how the operating conditions affected the driving power.

Mechanical Power

The output performance of the linear motor can be characterized by the mechanical power the motor can produce. The mechanical power can be found simply by the product of the load force and the average velocity of the motor. In Figure 4.12 the mechanical power output is shown as a function of load for cycle frequencies of 10, 30, and 50 hertz. The results found that the peak performance of the motor occurred under a load of approximately 100 newtons [23 lbs] and increased as the cycle frequency increased. The peak mechanical power produced by the motor was 310 mW corresponding to an average velocity of 3.1 mm/sec.

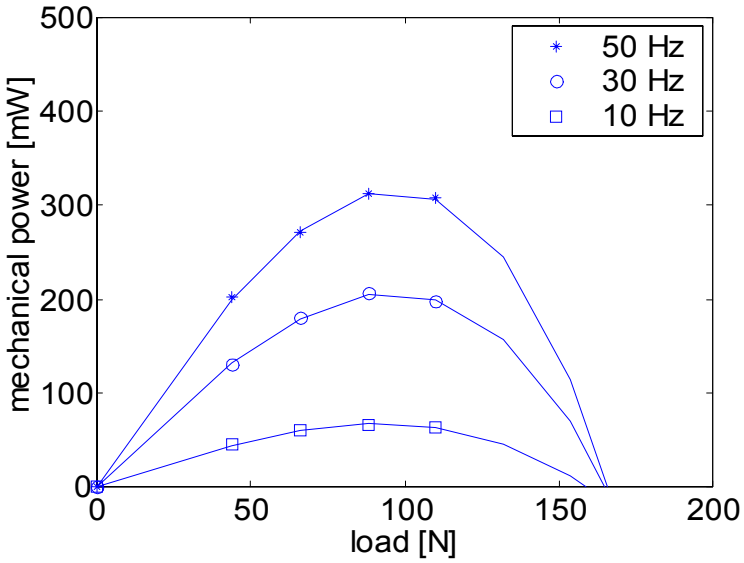

Figure 4.12: Mechanical power output as a function of motor load.

Driving Power

The power necessary to drive a piezoelectric linear motor can be found by the product of drive voltage (V_{drive}) and the drive current (I_{drive}). Due to the fact that piezoelectric materials behave similar to capacitors, the drive current can be represented by Equation 4.5. The equation shows that the amount of capacitive material used to create the motor will determine the current necessary to drive the motor.

$$I_{drive} = C\frac{dV_{drive}}{dt} \tag{4.5}$$

To test the power consumption of the motor, a switching amplifier used to power the extending actuator throughout the project was utilized. The switching amplifier has the limitation of a set output waveform. However, switching amplifiers are found to be much more efficient than linear amplifiers when driving capacitive loads. The switching amplifier is designed specifically for the application of driving capacitive material. Due to its design the amplifier is able to utilize the regenerative current produced by piezoelectric materials. The result is that there the amplifier supplies power to activate the actuator and the actuator returns a regenerative power back to the amplifier when deactivated. Therefore, the power consumed by the actuator is the difference between the power supplied and the regenerative power produced.

The results for the braking mechanisms (Figure 4.13a) found that an average power of 7.7 Watts was supplied to the actuator and average power of 3.3 Watts was consumed by the actuator at 50 Hz. The extending mechanism required a supplied power of 14.3 Watts and consumed an average power of 6.1 Watts at 50 Hz, as shown in Figure 4.13b. The results of the extending mechanism also show that the loading of the extending mechanism had little affect on the average power required to run the motor. Overall, the motor consumed an average power of 12.7 Watts at a drive frequency of 50 Hz. The results found that to reduce the power necessary to drive the phase two motor, the amount capacitive material used in the phase two motor will have to be reduced. While reducing the capacitive material used, the frequency at which a velocity is produced will also have to be maintained or reduced.

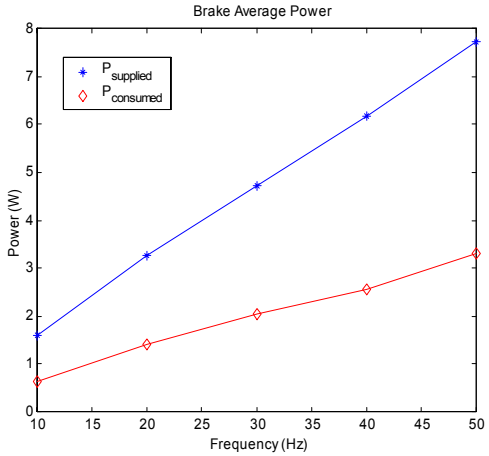

Figure 4.13a: Average power to drive one brake as a function of frequency.

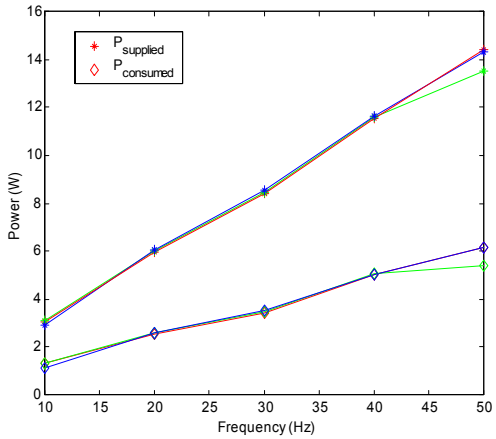

Figure 4.13b: Average power to drive the extender as a function of frequency.

Chapter 5

Conclusion

5.1 Summary of Phase One Model Design

The model created as part of phase one of the project, was found to predict the performance of the motor well. For the case in which the motor does not move against a load, the model worked very well. The results found that the model was able to predict the velocity of the motor for a cycle rate of 50 hertz within half a millimeter per second. For the case in which the motor does move against a load, the model did not work as well. The model did not account for the erratic losses that occurred during loaded movements. Overall, the results found that the model worked well for predicting the motor performance with less than a 20 pound load. However above 20 pounds, the erratic losses occurred more frequently causing the difference between the model and experimental to increase.

There are several applications in which the designed model could be found useful. The model will work well for predicting the loaded and unloaded performance of most incremental motor designs, that make use of frictional clamping mechanisms and that do not produce erratic losses due to clearances. The model can also predict the performance of an incremental motor that makes use of either a direct or amplified extending mechanism. By using the model, one can chose the desired characteristics of a direct or amplified actuator (stiffness, displacement, and blocked force) to be applied to a specific application. The design of the model allows the capability to alter each internal characteristic of an amplified actuator, such as the compliant amplification gain, compliant amplification stiffness, PZT actuator displacement, PZT actuator blocked force, and PZT actuator stiffness. Using these internal characteristics, one can design and build an amplified actuator for a specific

application. The model can also be helpful to predict the performance of a motor for several different input signals to the clamping and extending mechanisms. The waveform, peak voltage, and phasing between signals can all be altered within to model to predict changes in performance. The model created has been and will be a helpful tool in the design process of an incremental linear motor.

5.2 Summary of Phase One Motor Design

The motor created as part of phase one of the project was found to perform well compared to past incremental linear motor designs. A summary of the tested motor performance is shown in Table 5.1. The size, weight and power consumption of the motor was larger than desired, due to the low risk design for phase one. However, the unloaded speed of 4.9 mm/sec at 50 Hz and a stall load of 17 Kg proved satisfactory for a phase one design. Overall, the phase one design showed enough potential to ensure confidence that all goals of the project could be met by a phase two design.

Table 5.1: Summary of phase one motor results.

Parameter	Value	Units
Length	90	mm
Height	130	mm
Width	52	mm
Weight	0.8	Kg
Velocity (50 Hz)	5	mm/sec
Stall Load	17	Kg
Power Consumption (50 Hz)	13	Watts

To speculate the possible performance of the phase one design, the limitations caused by the amplifiers must be ignored. The input signal to the extending actuator can be increased from 130V to 180V, increasing the step size of the motor by a factor of approximately 1.4. Without the frequency limitation of the amplifiers, the next frequency limitation will be observed as the motor is driven to the frequency in which the clamping actuator activates at the point of full displacement of the extending actuator. Driving the motor above this frequency will decrease the step size produced by each cycle, due to the fact that the extending actuator will not be fully extended when the clamping actuator is activated. For the motor designed the maximum drive frequency can be estimated by the summation of

the time to produce full displacement (rise time) when the extending actuator contracts and extends. An estimate the rise time to reach the full response for a second order system can be found using Equation 5.1. During the contraction response, the actuator is subject to the load attached. For a motor load of 0 Kg to 11.3 Kg (25 lbs) the rise time was calculated to equal a time from 0.0002 to 0.0009 seconds. For the extending response the full response would occur at a rise time of approximately 0.0002 seconds. The summation of the time to complete the two motions leads to an approximation of a maximum run frequency of 2500 Hz for no load and 900 Hz for a load of 11.3 Kg. Assuming the velocity of the motor will increase linearly with frequency, an estimation of the possible increase in motor velocity from 50 Hz to an unloaded drive frequency of 2500 Hz would increase the velocity by a factor of 50. For the case of a 11.3 Kg load and a drive frequency of 900 Hz the velocity will increase by a factor of 18. The speculated performance of the unloaded motor to a 180V input signal at 2500 Hz would produce a velocity of approximately 250 mm/sec. The speculated loaded performance for a 11.3 Kg load and an input signal of 180V at 900 Hz would produce an approximate speed of 70 mm/sec. Note that the elimination of the amplifier limitations will not affect the stall load of the motor. The stall load was found to be dependent on the holding forces created by the brakes, the losses due to interface clearances, and the stiffness of the extending actuator.

$$T_r = \frac{(2.16\zeta + 0.60)}{\omega_{res}} \tag{5.1}$$

The phase one design process and experimental results has been helpful in finding weaknesses of the phase one design that could be improved upon in a phase two design. For example, improving the tolerances of the guide channel will allow a reduction in the amount of PZT material used in the clamping mechanisms. This reduction of PZT material will permit a smaller brake housing to be used, reducing the size and weight of the design. The power consumption of the clamping mechanisms would also be reduced by using less PZT material, allowing for an increase in motor efficiency. The four guide rods originally thought to be needed to support the extending mechanism were found to be an over design. The guide rods could be reduced to one or even eliminated depending on the application. The reduction or elimination of the guide rods will greatly reduce the size of the brake housings and will reduce the weight of the overall motor. The compliant extending actuator used

in the phase one design has the capability to produce the performance needed to meet the goals of the project. However, using a direct extending actuator would increase the motor's stiffness and performance under high loading conditions. The application of a direct extending actuator will likely prevent a reduction in the motor's height, but more importantly will allow for a reduction in motor length. A reduction in the length of the motor would reduce the size of the guide channel and improve the motor's ability to be packaged. The weakness that affected the phase one design the most was a result of the clearances at the clamping interface. The losses that occurred due to the interface clearances produced a drastic reduction in stall load to well under the project's goal of a 100 Lbs. These losses due to clearances will have to be eliminated to design a motor that will perform well under loaded conditions.

5.3 Contributions

Through out this paper the following contributions were presented:

- A design of an incremental linear motor in which the clamping mechanisms make use of PZT stacks preloaded using shape memory alloy wires.
- A design of an incremental linear motor in which the extending mechanism makes use a compliant amplified PZT actuator.
- A model of an incremental linear motor that makes use of a compliant amplified PZT actuator.

5.4 Future Work

The future work for the project consists of testing that was unable to be performed on the phase one motor due to time and equipment limitations. Once all phase one testing is completed the design, fabrication, and testing of a phase two motor will be performed. Before continuing onto phase two, testing of altered input signals will be performed to determine the influence on the motor's performance. Altering the waveform and phasing between input signal will lead to a optimal set of input signals that will produce the best motor performance. Additional testing of the phase one motor to higher frequencies will be

performed to observe the affects of resonance on the motor's performance and to find the optimal drive frequency for the motor (the resonant frequency). At the resonant frequency the motor will perform at its best; therefore, it may be desired to drive the motor at the resonant frequency and control velocity of the motor by adjusting the peak voltage of the extending actuator.

After all necessary testing of the phase one design is concluded, the phase two motor will be designed. The goals of the phase two design will be to reduce the size, weight, and power consumption of the current design, while improving its loaded and unloaded performance. A likely redesign of the phase one motor is presented in Figure 5.1. Note the dashed lines outline the size of the phase one motor. The phase two concept makes use of a flexure structure for the clamping mechanisms. Internal to each flexure structure the amount of piezoelectric material has been reduced to two PZT stacked actuators, each 2cm in length. By using a flexure structure the overall size of the clamping mechanisms can be easily reduced, while maintaining a preload on the PZT stacked actuators and preventing shear stress from being transferred to the actuators. Most importantly, the losses due to interface clearances have been eliminated. For the concept a direct actuator has been chosen for the extending mechanism. The direct actuator will allow for a slimmer design and will also increase the stiffness of the motor. Increasing the motor's stiffness will allow for higher drive frequencies to be achieved. This increase in drive frequency will increase the velocity in which the motor is able to obtain.

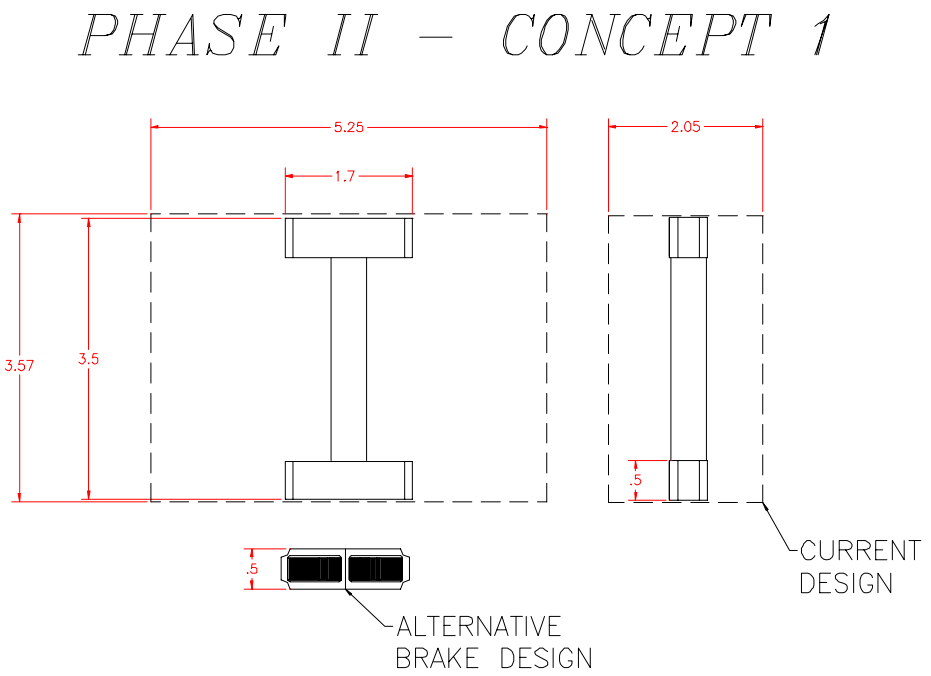

Figure 5.1: Phase two motor concept 1.

Bibliography

A. Hara, T. Horinchi, K. Yamada, S. Takahashi, and K. Nakamura, *Electomechanical Translation Device Comprising an Electrostrictive Driver of a Stacked Ceramic Capacitor Type*, **Patent #4,570,096**, 1986.

A.D. Brisbane, *Position Control Device*, **Patent #3,377,489**, 1968.

B. Edinger, M. Frecker, and J. Gardner, *Dynamic Modeling of an Innovative Piezoelectric Actuator for Minimally Invasive Surgery*, **Adaptive Structures and Materials Systems (ASME)**, Vol. 59, pp. 183–188, 1999.

B. Zhang and Z. Zhu, *Design of an Inchworm-Type Linear Piezomotor*, **SPIE Proceedings**, Vol. 2190, pp. 528–539, 1994.

Cedrat_Recherche, *Piezo Actuators Catalogue*, **Version 2.1**, 2000.

C.G. O'Neill and C.E. Foster, *Electromotive Actuator*, **Patent #4,219,755**, 1980.

G. Carman, Q. Chen, D. Yao, and C. Kim, *Mesoscale Actuator Device: Micro Interlocking Mechanism to Transfer Macro Load*, **Sensors and Actuators**, Vol. 73, pp. 30–36, 1999.

Galante, T., 1997, **Design and Fabrication of a High Authority Linear Piezoceramic Actuator: The PSU H3 Inchworm**, M.S. Thesis, The Pennsylvania State University.

G.L. Locher, *Micrometric Linear Actuator*, **Patent #3,296,467**, 1967.

G.R. Stibitz, *Incremental Feed Mechanisms*, **Patent #3,138,749**, 1964.

G.V. Galutva, *Device For Precision Displacement of a Solid Body*, **Patent #3,684,904**, 1972.

J. Frank, G. Koopmann, W. Chen, and G. Lesieutre, *Design and Performance of a High Force Piezoelectric Inchworm Motor*, **SPIE Proceedings**, Vol. 3668, pp. 717–723, 1999.

J. Oliver, R. Neurgaoukar, J. Nelson, and C. Bertolini, *Moving Linear Piezoelectric Motor for Vehicle Appications*, **Patent #5,780,957**, 1998.

J.E. Miesner and J.P. Teter, *Piezoelectric/Magnetosrictive Resonant Inchworm Motor*, **SPIE Proceedings**, Vol. 2190, pp. 520–527, 1994.

Oberg and Ryffell, **Machinery's Handbook**, 26th Edition, Industrial Press INC., New York, 2000.

Physik_Instrumente, *NanoPositioning*, **Catalog # 114**, 1998.

Piezomechanik, *Piezoelectric and Electrostrictive Stack Actuators*, **Catalog**, 2000.

Piezo_Systems, *Introduction to Piezoelectricity*, **Catalog # 4**, 2000.

R.A. Bizzigotti, *Electromechanical Translation Apparatus*, **Patent #3,902,085**, 1975.

S. Canfield, B. Edinger, M. Frecker, and G. Koopmann, *Design of Piezoelectric Inchworm Actuator and Compliant End-Effector for Minimally Invasive Surgery*, **SPIE Proceedings**, Vol. 3668, pp. 835–843, 1999.

S. Hsu, A. Arbor, and A. Blatter, *Transducer*, **Patent #3,292,019**, 1966.

S. Lee and M. Esashi, *Design of the Electrostatic Linear Microactuator Based on the Inchworm Motion*, **Mechatronics**, Vol. 5, No. 8, pp. 963–972, 1995.

Shields, J., **Basic Piezoelectricity**, Howard W. Sams and Co., Inc., Indianapolis, Indiana, 1966.

T. Fujimoto, *Linear Motor Driving Device*, **Patent #4,736,131**, 1988.

T. Murata, *Drive Apparatus and Motor Unit Using The Same*, **Patent #4,947,077**, 1990.

T. Pandell and E. Garcia, *Design of a Piezoelectric Caterpillar Motor*, **Proceedings of the ASME Aerospace Division**, Vol. 52, pp. 627–648, 1996.

T. Shibuya, *Piezoelectric Motor*, **Patent #4,777,398**, 1988.

W.G. May, Jr., *Piezoelectric Electromechanical Translation Apparatus*, **Patent #3,902,084**, 1975.

Z. Zhu and B. Zhang, *Developing a Linear Piezomotor With Nanometer Resolution and High Stiffness*, **IEEE/ASME Transactions on Mechatronics**, Vol. 2, No. 1, pp. 22–29, 1997.

Appendix A

A.1 MatLab Code

A.1.1 Parameters for Ideal Motor Simulation

```
%  Parameters For Ideal Amplified Extender Model

clear all;

%%%%%%%%%%%%%%%%%%%%%%%%%%%%%%%%%%
%  SIMULINK Model Parameters
%%%%%%%%%%%%%%%%%%%%%%%%%%%%%%%%%%

f = 10;             %(Hz)      %drive frequency
mus = .8;                      %static coefficient of friction
mud = .4;                      %dynamic coefficient of friction
m_load = 0;         %(kg)      %applied load
F_b = 3500;         %(N)       %blocked force for brake actuators
V_b = 150;          %(V)       %max input voltage for brake actuators
D_b = 79*10^-6;     %(m)       %max displacement of brake actuators
F_act = 1400;       %(N)       %blocked force of compliant amplified actuator
V_act = 180;        %(V)       %max input voltage for compliant amplified actuator
D_act = 150*10^-6; %(m)        %max displacement of compliant amplified actuator
K_act = 11.7*10^6; %(N/m)      %stiffness of overall compliant amplified actuator
```

```
Cact = 90;          %(kg/s)    %damping coefficient of compliant amplified actuator
M1 = 0.4705;        %(kg)      %mass of brake 1
M2 = 0.4855;        %(kg)      %mass of brake 2
l1 = 1;
l2 = 3;                        %amplification gain of compliant structure

Kvb1 = F_b/V_b;                      %(N/V)    %voltage constant for brake 1 actuator
Kvb2 = F_b/V_b;                      %(N/V)    %voltage constant for brake 2 actuator
Keb1 = F_b/D_b;                      %(N/m)    %stiffness of brake 1 actuator
Keb2 = F_b/D_b;                      %(N/m)    %stiffness of brake 2 actuator
Kvpzt = F_act*l2/V_act;              %(N/V)    %voltage constant for PZT stack
                                     %           internal to amplified actuator
Kepzt = F_act*l2/(D_act/l2);         %(N/m)    %stiffness of PZT stack internal
                                     %           to amplified actuator
Kcomp = 2/((1/K_act)-(l2^2/Kepzt)); %(N/m)    %stiffness of compliant structure
g = 9.82;                            %(m/s^2)  %gravity constant

%  Equivalent voltage constant for extending actuator
Kv_act = (Kcomp*Kvpzt*l1*l2)/(2*Kepzt*l1^2+Kcomp*l2^2)

%  Equivalent stiffness of extending actuator
Ke_act = (Kcomp*Kepzt*l1^2)/(2*Kepzt*l1^2+Kcomp*l2^2)
```

A.1.2 Brake 1 Code

```
%  Determination of Brake 1 State
%  Code connected to MatLab function in SIMULINK Model

function y1 = B1(u)

%  Inputted Parameters
```

```
mus = u(1);                          %static friction coefficient
mud = u(2);                          %dynamic friction coefficient
Fbrake1_in = u(3);                   %current frictional force applied by brake 1
Fext = u(4);                         %force applied to brake 1 by extender
Fdamping = u(5);                     %damping force applied to brake 1
Fspring = u(6);                      %spring force applied to brake 1

%  brake forces
Fbrake1_s = Fbrake1_in*mus;          %static frictional force
Fbrake1_d = Fbrake1_in*mud;          %slipping frictional force

%  inertial force
Force1 = Fspring+Fdamping-Fext;

%  when brake is not activated
if Fbrake1_in == 0
   X1_mem = 0;
   Fbrake1 = 0;
end

%  when brake is activated
if abs(Fbrake1_in) > 0

%  brake force greater than opposing forces
if abs(Force1) <= abs(Fbrake1_s)
    X1_mem = 1;
    Fbrake1 = -Force1;
end

%  brake force less than opposing forces
if abs(Force1) > abs(Fbrake1_s)
```

```
    X1_mem = 0;
    Fbrake1 = Fbrake1_d*(-Force1/abs(Force1));
end
end

%  Brake 1 force and condition output
y1 = [Fbrake1;X1_mem];
```

A.1.3 Brake 2 Code

```
%  Determination of Brake 2 State
%  Code connected to MatLab function in SIMULINK Model

function y2 = B2(u)

Fspring = u(1);                %spring force applied to brake 2
Fdamping = u(2);               %damping force applied to brake 2
Fext = u(3);                   %force applied to brake 2 by extender
Load = u(4);                   %load force applied to brake 2
Fbrake2_in = u(5);             %current frictional force applied by brake 2
mus = u(6);                    %static friction coefficient
mud = u(7);                    %dynamic friction coefficient

%  brake forces
Fbrake2_s = Fbrake2_in*mus;    %static frictional force
Fbrake2_d = Fbrake2_in*mud;    %slipping frictional force

%  inertial force
Force2 = -Fspring-Fdamping+Fext-Load;

%  when brake is not activated
```

```
if Fbrake2_in == 0
   X2_mem = 1;
   Fbrake2 = 0;
end

%  when brake is activated
if abs(Fbrake2_in) > 0

%  brake force greater than opposing forces
if abs(Force2) <= abs(Fbrake2_s)
    X2_mem = 0;
    Fbrake2 = -Force2;
end

%  brake force less than opposing forces
if abs(Force2) > abs(Fbrake2_s)
    X2_mem = 1;
    Fbrake2 = Fbrake2_d*(-Force2/abs(Force2));
   end
end

%  Brake 1 force and condition output
y2 = [Fbrake2;X2_mem];
```

A.2 Simulink Block Diagram

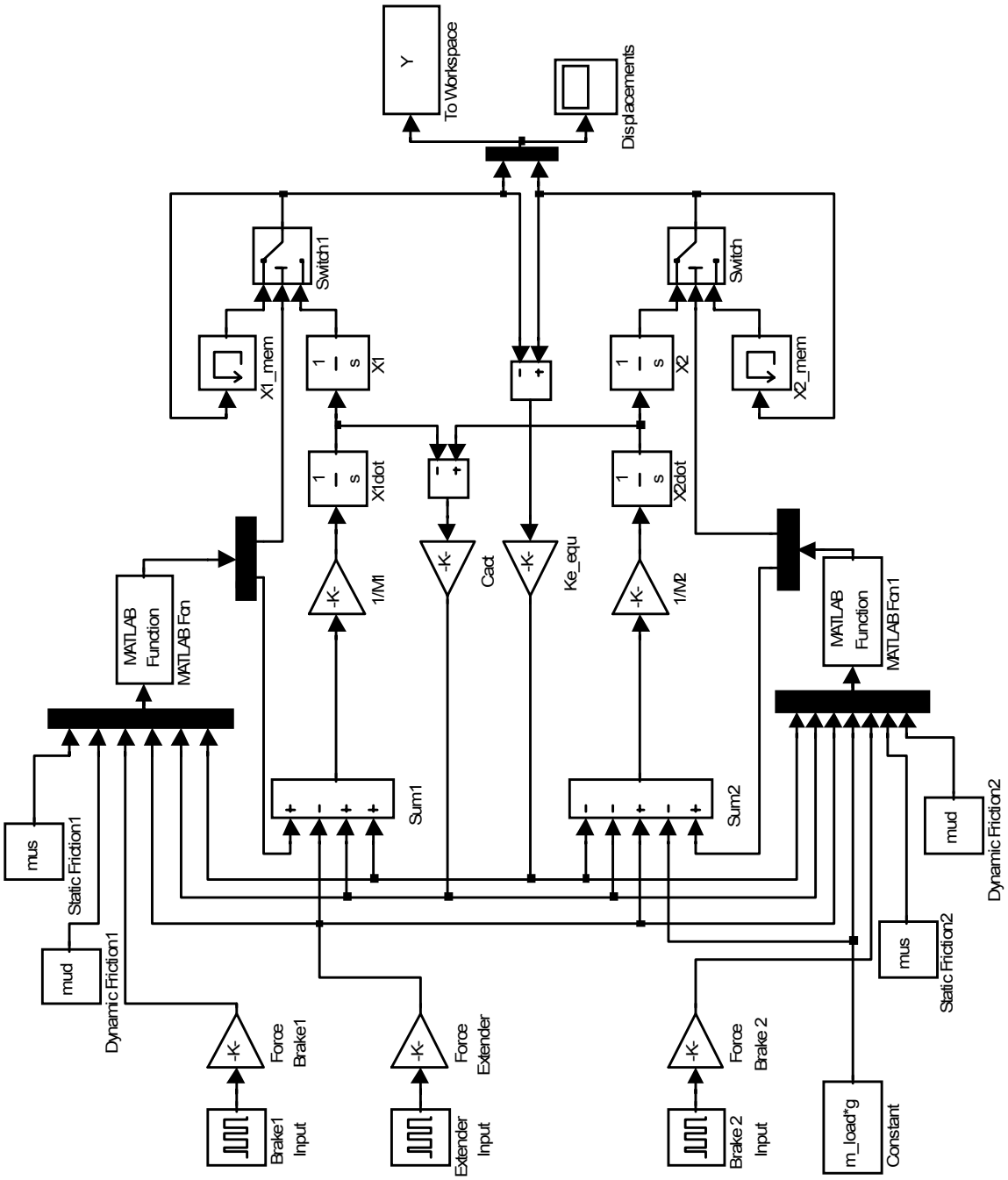

Appendix B

B.1 Detailed Drawings

Drawings Presented:

- Button Interface, End Cap, and Bushing Detail
- Center Support
- Preloaded Actuator Assembly
- Brake Housing
- Brake Housing Cover
- Guide Shaft Detail
- Roller Assembly

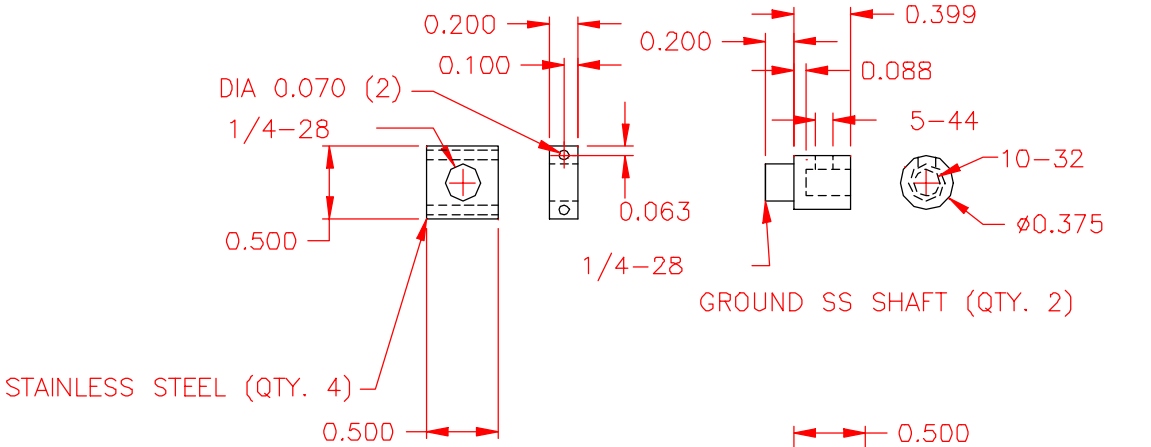

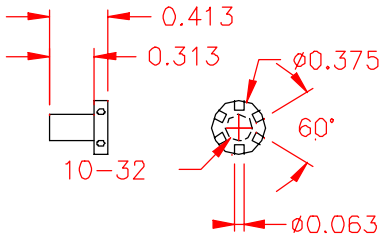

STAINLESS STEEL (QTY. 2)

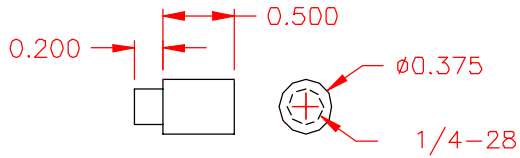

GROUND SS SHAFT (QTY. 2)

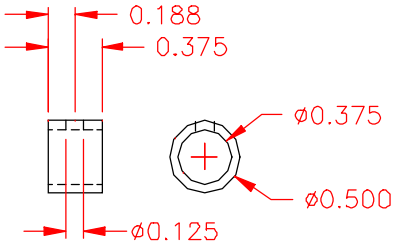

SAE 841 OIL IMPR. BRONZE (QTY. 4)

NOTE:

1. DIMENSIONS IN INCHES
   UNLESS OTHERWISE NOTED

DRILL AND REAM HOLES AFTER PRESSED INTO HOUSING

BUTTON DETAIL

SCALE 3/4:1

REV. 01 02/12/01

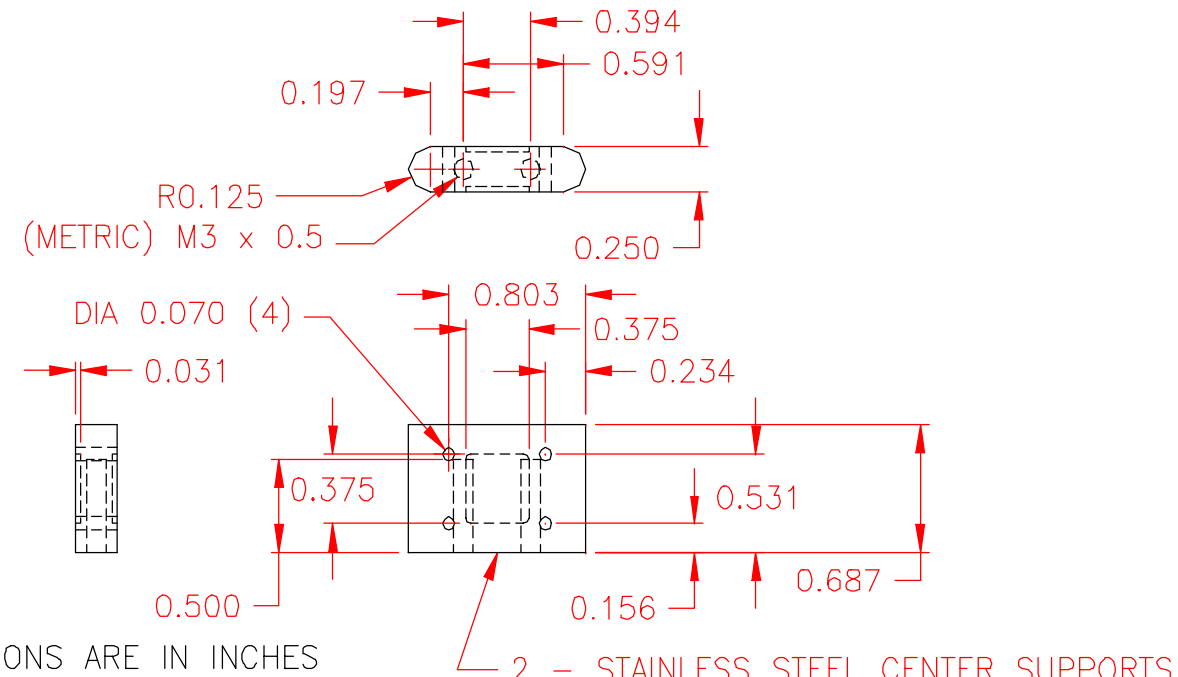

NOTE:
1. DIMENSIONS ARE IN INCHES UNLESS OTHERWISE NOTED.

CENTER SUPPORT DETAIL

SCALE 1:1
REV. 01 02/12/01
REV. 02 02/25/01

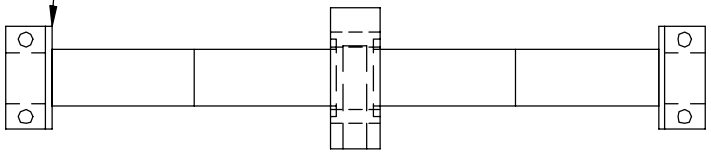

ACTUATOR #1

SIDE #1 (PZT #2, PZT #8)
SIDE #2 (PZT #3, PZT #6)

ACTUATOR #2

SIDE #1 (PZT #4, PZT #9)
SIDE #2 (PZT #5, PZT #7)

NOTE:

POSITION STACKS SUCH THAT THE WIRE LEADS ARE POINTING TOWARD THE CENTER OF THE ASSEMBLY

PRELOAD ASSEMBLY DETAIL

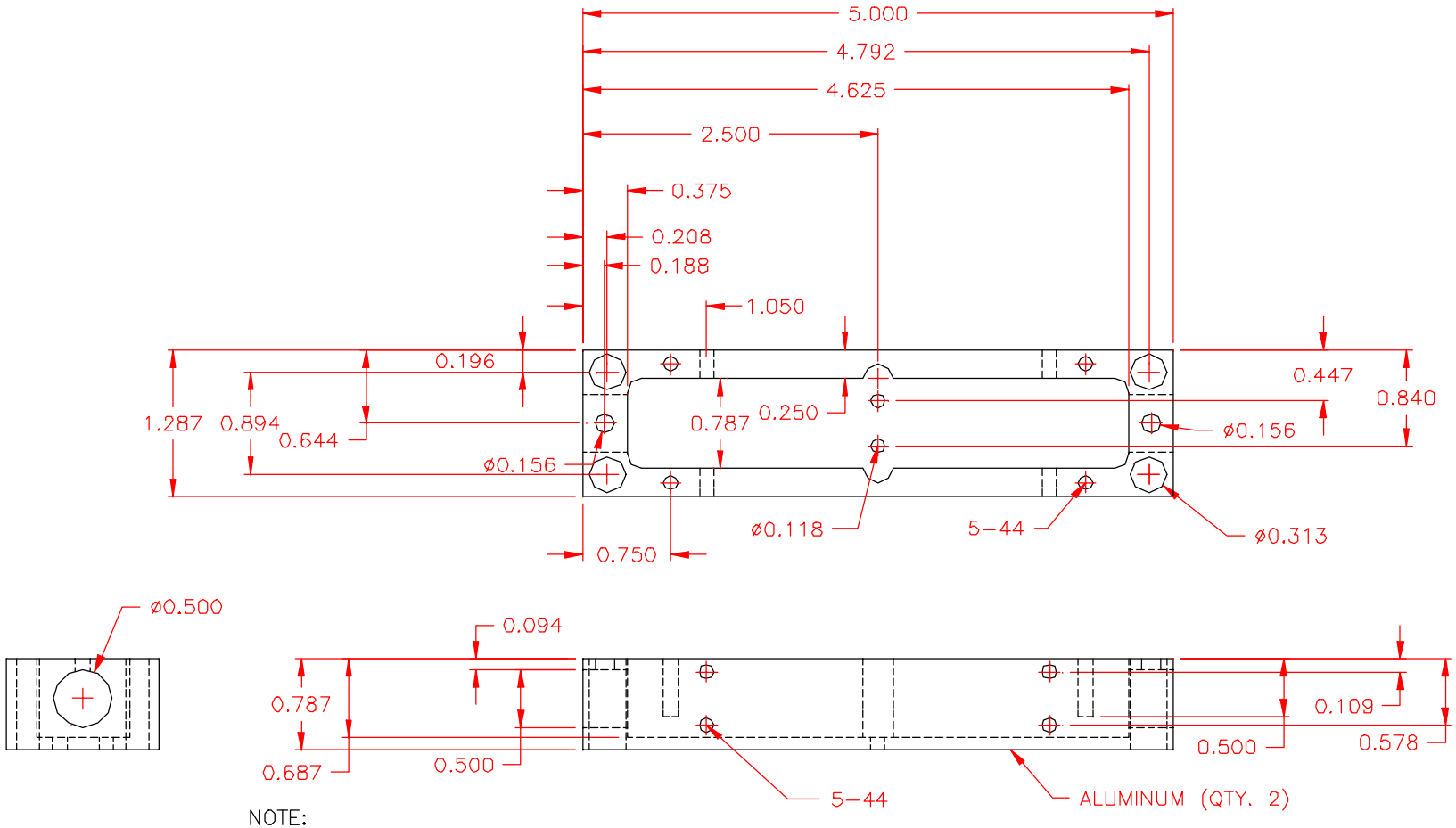

NOTE:
1. HOUSING ACCESS PLATE REMOVED FOR CLARITY
2. DIMENSIONS IN INCHES UNLESS OTHERWISE NOTED

HOUSING DETAIL

SCALE 3/4:1
REV. 01 01/23/01
REV. 02 02/12/01

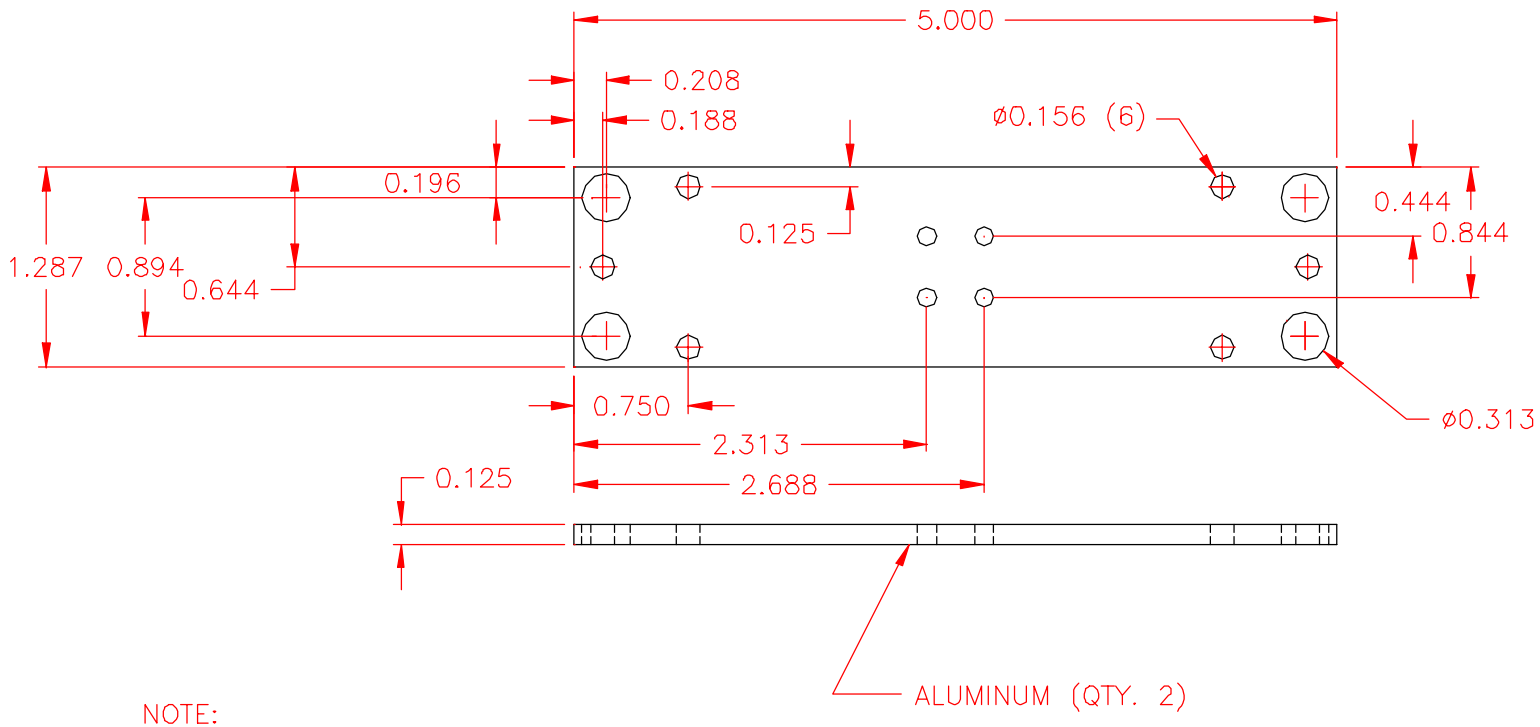

NOTE:

1. DIMENSIONS IN INCHES
   UNLESS OTHERWISE NOTED

COVER DETAIL

SCALE 1:1
REV. 01 02/12/01

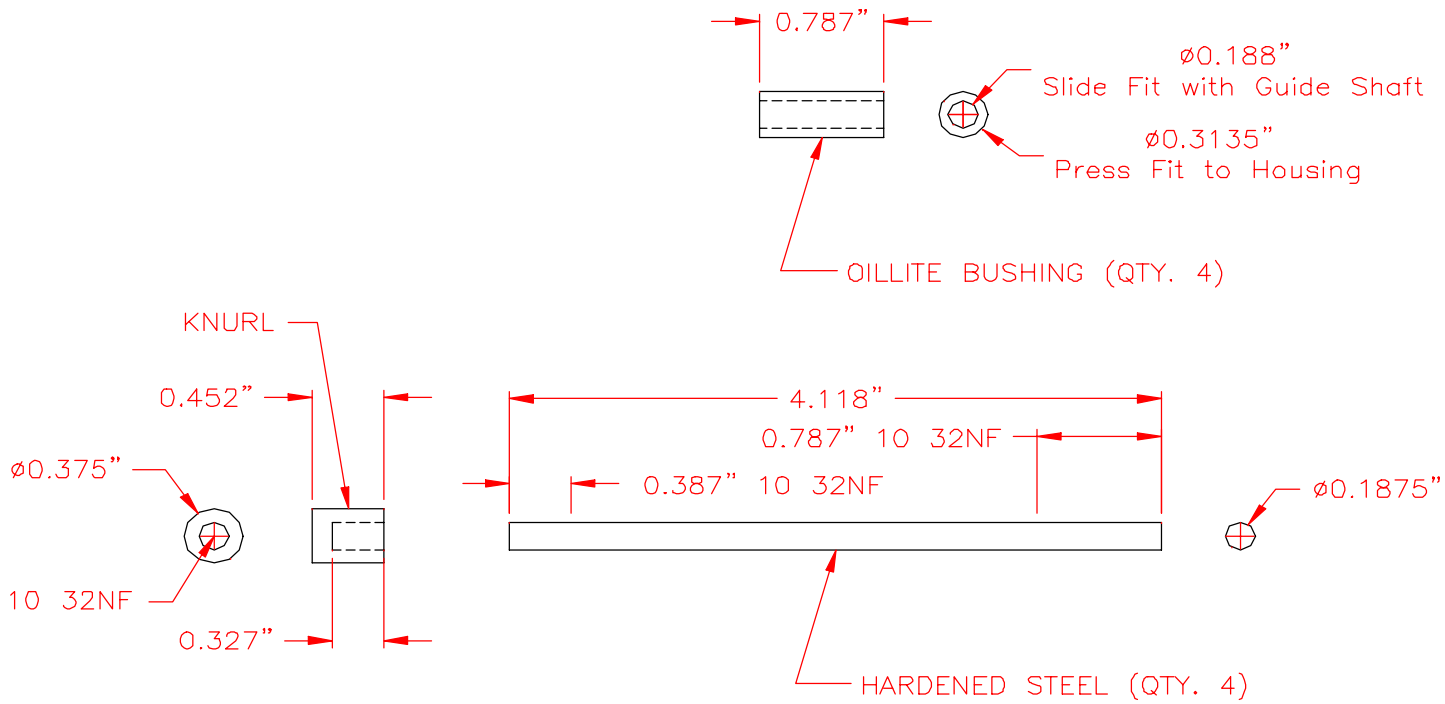

GUIDE SHAFT DETAIL

SCALE 1:1
REV. 01 02/12/01

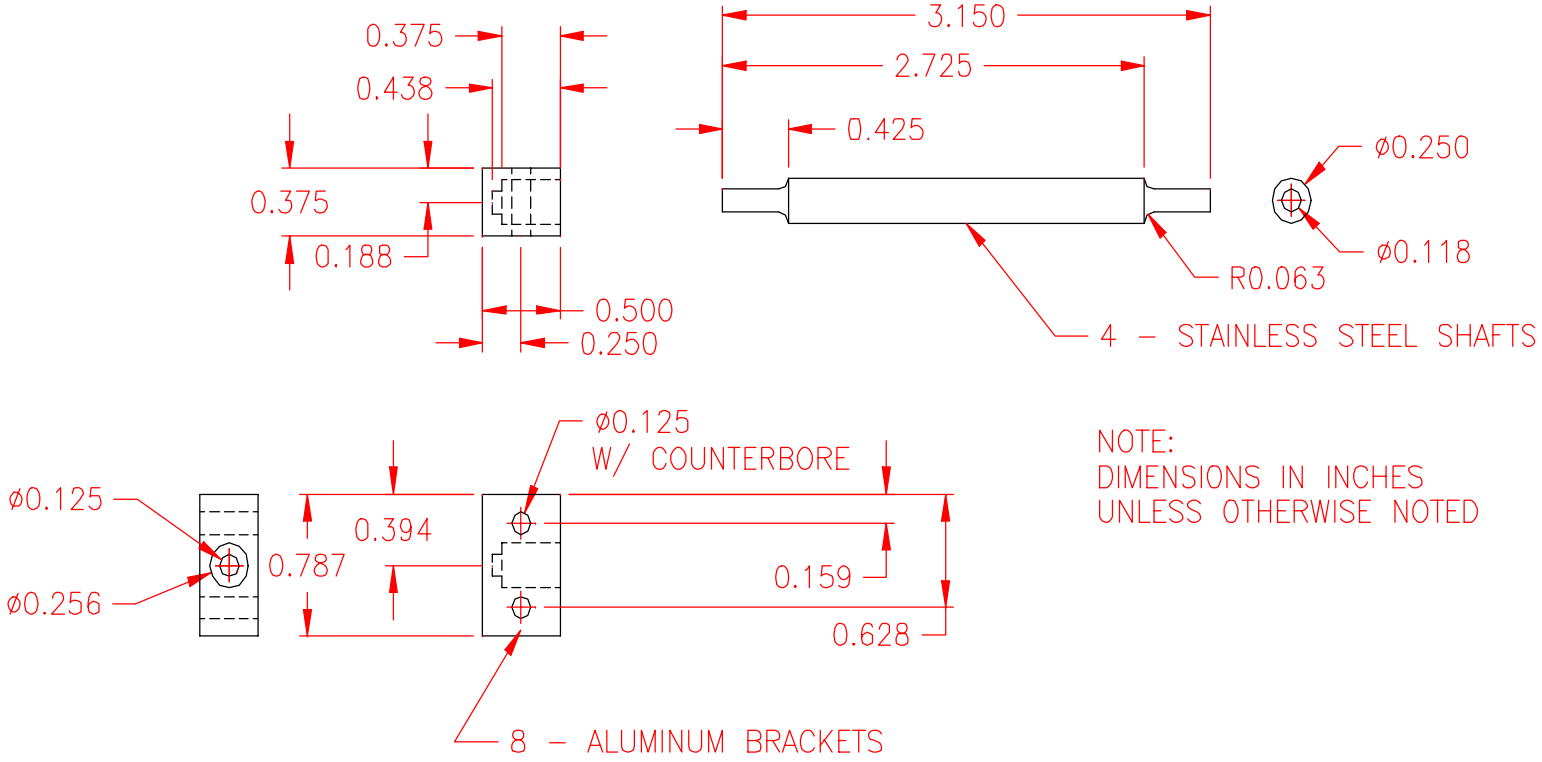

NOTE:
DIMENSIONS IN INCHES
UNLESS OTHERWISE NOTED

ROLLER MECHANISM DETAIL

SCALE 1:1
REV. 01 02/12/01

Vita

Mark Edward Vaughan, son of Donald and Martha Vaughan, was born on August 26, 1978, in Richmond Virginia. He attended and graduated from Meadowbrook High School in June of 1996. He enrolled in the Mechanical Engineering department at Virginia Commonwealth University later that August. He transferred to Virginia Tech one year later, and graduated in May 2000 with a B.S. in Mechanical Engineering. Staying at Virginia Tech for another year and a half, he pursued a Masters of Science in Mechanical Engineering with the Center for Intelligent Material Systems and Structures (CIMSS), concentrating on the application of piezoelectrics in motor design.

Permanent Address: 1202 Toms Creek Rd. Apt 102A
Blacksburg, VA 24060

This thesis was typeset with LaTeX 2$_\varepsilon$[1] by the author.

[1] LaTeX 2$_\varepsilon$ is an extension of LaTeX. LaTeX is a collection of macros for TeX. TeX is a trademark of the American Mathematical Society. The macros used in formatting this thesis were written by Greg Walker, Department of Mechanical Engineering, Virginia Tech.